

Study of the Cosmic Rays and Interstellar Medium in Local H I Clouds using *Fermi*-LAT  
Gamma-Ray Observations

T. MIZUNO,<sup>1</sup> S. ABDOLLAHI,<sup>2</sup> Y. FUKUI,<sup>3</sup> K. HAYASHI,<sup>3</sup> T. KOYAMA,<sup>2</sup> A. OKUMURA,<sup>4</sup> H. TAJIMA,<sup>4,5</sup>  
AND H. YAMAMOTO<sup>3</sup>

<sup>1</sup>*Hiroshima Astrophysical Science Center, Hiroshima University, 1-3-1 Kagamiyama, Higashi-Hiroshima, Hiroshima, 739-8526, Japan*

<sup>2</sup>*Department of Physical Sciences, Hiroshima University, Higashi-Hiroshima, Hiroshima 739-8526, Japan*

<sup>3</sup>*Department of Physics and Astrophysics, Nagoya University, Nagoya, Aichi 464-8602, Japan*

<sup>4</sup>*Institute for Space-Earth Environmental Research, Nagoya University, Nagoya, Aichi 464-8601, Japan*

<sup>5</sup>*W. W. Hansen Experimental Physics Laboratory, Kavli Institute for Particle Astrophysics and Cosmology, Department of Physics and SLAC National Accelerator Laboratory, Stanford University, Stanford, CA 94305, USA*

(Received January 1, 2018; Revised January 7, 2018; Accepted February 5, 2020)

Submitted to ApJ

ABSTRACT

An accurate estimate of the interstellar gas density distribution is crucial to understanding the interstellar medium (ISM) and Galactic cosmic rays (CRs). To comprehend the ISM and CRs in a local environment, a study of the diffuse  $\gamma$ -ray emission in a mid-latitude region of the third quadrant was performed. The  $\gamma$ -ray data in the 0.1–25.6 GeV energy range of the *Fermi* Large Area Telescope (LAT) and other interstellar gas tracers such as the HI4PI survey data and the *Planck* dust thermal emission model were used, and the northern and southern regions were analyzed separately. The variation of the dust emission  $D_{\text{em}}$  with the total neutral gas column density  $N_{\text{H}}$  was studied in high dust-temperature areas, and the  $N_{\text{H}}/D_{\text{em}}$  ratio was calibrated using  $\gamma$ -ray data under the assumption of a uniform CR intensity in the studied regions. The measured integrated  $\gamma$ -ray emissivities above 100 MeV are  $(1.58 \pm 0.04) \times 10^{-26}$  photons  $\text{s}^{-1} \text{sr}^{-1} \text{H-atom}^{-1}$  and  $(1.59 \pm 0.02) \times 10^{-26}$  photons  $\text{s}^{-1} \text{sr}^{-1} \text{H-atom}^{-1}$  in the northern and southern regions, respectively, supporting the existence of a uniform CR intensity in the vicinity of the solar system. While most of the gas can be interpreted to be H I with a spin temperature of  $T_{\text{S}} = 125$  K or higher, an area dominated by optically thick H I with  $T_{\text{S}} \sim 40$  K was identified.

*Keywords:* cosmic rays — gamma rays: ISM — ISM: general

1. INTRODUCTION

High-energy  $\gamma$ -rays (energy  $E \gtrsim 100$  MeV) are produced by interactions of cosmic-ray (CR) particles with the gas and the radiation fields in the interstellar medium (ISM). Because the ISM is essentially transparent to those  $\gamma$ -rays (e.g., [Moskalenko et al. 2006](#)), observations of high-energy  $\gamma$ -rays are a useful probe of CRs and other components of the ISM. Assuming an electron-to-proton ratio in the interstellar space to be  $\sim 100$  at 10 GeV (the value measured at the Earth),  $\gamma$ -rays produced via nucleon-nucleon interactions is dominant compared to those by electron bremsstrahlung. Because the  $\gamma$ -ray production cross section is independent of the chemical or thermodynamic state of the ISM gas, if the gas column density is well-established at medium to high Galactic latitudes, then the CR proton intensity can be inferred under the assumption of a uniform intensity and a known contribution of heavier elements (and an uniform electron-to-proton ratio).

Usually, the distribution of neutral atomic hydrogen (H I) is measured via 21-cm line surveys (e.g., [Dickey & Lockman 1990](#)) by assuming the optically thin approximation or a uniform spin temperature ( $T_S$ ), and the distribution of molecular hydrogen (H<sub>2</sub>) is indirectly estimated from the carbon monoxide (CO) line-emission surveys (e.g., [Dame et al. 2001](#)) assuming a linear conversion factor (usually called  $X_{CO}$ ). Although the volume fraction of ionized gas is large, its column density is usually small (e.g., [Ferriere 2001](#)) and can be neglected compared to the neutral gas. The total neutral gas column density can also be indirectly estimated from dust using the extinction, reddening, or emission (e.g., [Bohlin et al. 1978](#)). A significant amount of gas not traced properly via H I and CO surveys in the solar neighborhood has been revealed by combining the EGRET  $\gamma$ -ray data, H I, CO, and dust extinction maps and has been referred to as “dark gas” ([Grenier et al. 2005](#)). Its column density is comparable to that of H<sub>2</sub> gas traced by CO. Subsequently, the work by [Grenier et al. \(2005\)](#) has been confirmed and improved in terms of significance and accuracy by recent observations of Galactic diffuse  $\gamma$ -rays by *Fermi* Large Area Telescope (LAT; [Atwood et al. 2009](#)), as exemplified by [Abdo et al. \(2010\)](#) and [Ackermann et al. \(2011, 2012b\)](#). In addition, the *Planck* mission has provided an all-sky dust thermal emission model ([Planck Collaboration XIX 2011](#); [Planck Collaboration XI 2014](#)) that is useful for the study of the ISM gas distribution because of its precision and high angular resolution.

However, both  $\gamma$ -ray emission and dust emission  $D_{em}$  (or extinction/reddening) studies have limitations, and therefore the ISM gas distribution (and CR intensity in the interstellar space) remains uncertain even in the solar neighborhood. On the  $\gamma$ -ray side, measurements suffer from low photon statistics to trace the ISM gas distribution at high angular resolution, contamination from point sources, and background due to inverse Compton (IC) emission and isotropic background signal at high Galactic latitude. On the dust side, a procedure to convert  $D_{em}$  into the total neutral gas column density ( $N_H$ ) has not yet been established. For example, [Fukui et al. \(2015\)](#) compared the integrated H I 21-cm line intensity ( $W_{HI}$ ) and the *Planck* dust optical depth at 353 GHz ( $\tau_{353}$ ) in their all-sky data analysis (with a low latitude region ( $|b| \leq 15^\circ$ ) and several other areas masked) and interpreted the strong dust temperature ( $T_d$ ) dependence of the  $W_{HI}$  to  $\tau_{353}$  ratio as a significant amount of optically thick H I. Meanwhile, the [Planck Collaboration XI \(2014\)](#) found that the dust radiance  $R$  (integrated intensity) correlated well with  $W_{HI}$  over a wide range of  $T_d$  in the diffuse ISM and proposed that it would be a better tracer of the dust (and the total gas) column density. We also note that the dust-to-gas conversion may be affected by dust and gas properties that can vary over the region. In particular the uncertainty on the H I gas  $T_S$  have not been fully accounted for in previous studies of  $\gamma$ -ray data (e.g., [Abdo et al. 2010](#); [Ackermann et al. 2011, 2012b](#)). This

contributes to the uncertainties on the total ISM gas column density and then on the CR intensity distribution estimates (see, e.g., Grenier et al. 2015).

In this paper, we describe a detailed analysis of the *Fermi*-LAT data for a mid-latitude region of the third quadrant (see Section 2.1 and Appendix A for details of the region definition). Two regions of interest (ROIs), spanning northern and southern Galactic latitude ranges ( $22^\circ \leq |b| \leq 60^\circ$ ), do not contain any known large molecular clouds. Most of the atomic hydrogen is expected to be within 1 kpc of the solar system and therefore the dust-to-gas ratio and CR intensity are expected to be uniform due to the ROIs covering medium-to-high Galactic latitudes. They were analyzed in an early publication of *Fermi*-LAT analysis using six months of data (Abdo et al. 2009b) to study the CR intensity in the vicinity of the solar system. We now aim to better constrain the ISM gas distribution and the CR intensity/spectrum using eight years of *Fermi*-LAT data and newly available gas data such as the HI4PI survey data (HI4PI Collaboration 2016) and the *Planck* dust emission models. In the light of studies by Fukui et al. (2015) and Planck Collaboration XI (2014), we consider both  $\tau_{353}$  and  $R$ .

This paper is organized as follows. We describe the properties of the ISM tracers ( $W_{\text{HI}}$  for the HI4PI survey and  $R$  or  $\tau_{353}$  for *Planck*) in the studied regions in Section 2 and the  $\gamma$ -ray observations, data selection, and modeling in Section 3. To model the  $\gamma$ -ray data we take into account the neutral gas component ( $W_{\text{HI}}$ ,  $R$ , or  $\tau_{353}$ ), IC emission, isotropic background, emission from the Sun and Moon, and  $\gamma$ -ray point sources. We also include ionized gas contribution as a fixed component. The results of the data analysis are presented in Section 4, in which we use the *Fermi*-LAT  $\gamma$ -ray data as a robust tracer of  $N_{\text{H}}$ . We discuss the ISM and CR properties of the studied region in Section 5. A summary of this study and future prospects are presented in Section 6.

## 2. ISM GAS TRACER PROPERTIES AND MAP PREPARATION

### 2.1. *Properties of the ISM Gas in the ROI*

Prior to preparing templates of the ISM gas for the  $\gamma$ -ray data analysis, we investigated the properties of their tracers. As neutral gas tracers, we prepared dust maps and a  $W_{\text{HI}}$  map stored in a HEALPix (Górski et al. 2005) equal-area sky map of order  $9^1$  (with a mean spacing of  $6'.9$  that is commensurate with the  $\sim 5'$  resolution of the Planck dust maps.) We used the *Planck* dust maps (of  $R$ ,  $\tau_{353}$ , and  $T_{\text{d}}$ ) from the public data release 1 (version R1.20)<sup>2</sup> described by Planck Collaboration XI (2014).<sup>3</sup> Assuming a uniform dust temperature along the line of sight, they constructed maps by modeling the dust thermal emission with a single modified black body (for details of their procedure, see Planck Collaboration XI 2014). As described in Planck Collaboration XI (2014), the dust optical depth is the product of the dust opacity and the total neutral gas column density  $N_{\text{H}}$ . Therefore, if the dust-to-gas ratio and dust cross section at 353 GHz are spatially constant,  $\tau_{353}$  is proportional to  $N_{\text{H}}$ . The dust radiance  $R$  is also expected to trace the total gas column density because it is proportional to  $N_{\text{H}}$  under the assumption that the dust-to-gas ratio, the optical and UV absorption cross section of the dust, and the interstellar radiation field are spatially uniform. These hypotheses have to be tested because dust evolution models predict that the dust emission properties change across the ISM (e.g., Roy et al. 2013; Ysard et al. 2015); which severely discourages the use of a single conversion factor without verification. For this reason we investigate the change in the  $N_{\text{H}}-D_{\text{em}}$  relationship with dust properties using  $\gamma$ -ray data (Section 4). We analyzed the northern ROI ( $200^\circ \leq l \leq 260^\circ$  and  $22^\circ \leq b \leq 60^\circ$ ) and the southern ROI ( $210^\circ \leq l \leq 270^\circ$  and  $-60^\circ \leq b \leq -22^\circ$ ). The northern ROI is identical to that adopted by Abdo et al. (2009b) but the southern ROI is shifted by  $10^\circ$  (see below). To construct the  $W_{\text{HI}}$  map, we used the HI4PI survey data (HI4PI Collaboration 2016) integrated over the full velocity range of the survey (from  $-600$  to  $600$  km s $^{-1}$ ). In the  $W_{\text{HI}}$  map, we identified several bright radio sources and intermediate velocity clouds (e.g., Wakker 2001). We removed these radio sources from the  $W_{\text{HI}}$  map by filling them with the average of the peripheral pixels. We also identified an area where the  $W_{\text{HI}}-D_{\text{em}}$  relation is affected by the contamination of an intermediate velocity cloud, and masked the area when studying the  $W_{\text{HI}}-D_{\text{em}}$  relation and  $\gamma$ -ray data analysis. We also masked the Orion-Eridanus superbubble (e.g., Ochsendorf et al. 2015) because the CR and ISM properties inside the bubble can be appreciably different from those in other areas (see Appendix A for details). To compensate the loss of photon statistics because of the mask, we shifted the longitude of the southern ROI by  $10^\circ$  toward the positive direction (i.e., away from the mask) from that of Abdo et al. (2009b). In the *Planck* dust maps, we identified several spots with high  $R/\tau_{353}$  ratios and high  $R$ . They are likely infrared sources and were removed from the dust maps by filling them with the average of the peripheral pixels (see Appendix B). Finally, we examined the *Planck* type 3 CO map that has the highest signal-to-noise ratio among three types of the map (Planck Collaboration XIII 2014) and confirmed that there is no strong CO 2.6-mm emission in our ROI (see Appendix C). We identified a weak spot at  $(l, b) \sim (221^\circ.4, 45^\circ.1)$ . This spot can also be seen in the  $R$  and  $\tau_{353}$  maps and is therefore likely to be an infrared source. Therefore, we removed

<sup>1</sup> This corresponds to the total number of pixels of  $12 \times (2^9)^2 = 3145728$ . (9 comes from the resolution index.)

<sup>2</sup> [http://irsa.ipac.caltech.edu/data/Planck/release\\_1/all-sky-maps/](http://irsa.ipac.caltech.edu/data/Planck/release_1/all-sky-maps/)

<sup>3</sup> We note that a specific choice of the data release version is not crucial to constrain the  $N_{\text{H}}$  distribution and CR intensity because we use  $\gamma$ -ray data as a robust tracer of the ISM gas as described in Section 4. We also confirmed that the *Planck* public data release 2 gives similar  $W_{\text{HI}}-D_{\text{em}}$  relationships as those in Section 2.1 (stronger  $T_{\text{d}}$  dependence and non-linearity for the case of  $\tau_{353}$  in the northern and southern regions, respectively).



the source from the dust maps by filling the source area with the average of the peripheral pixels, and do not consider CO-bright  $\text{H}_2$  in constructing gas models hereafter.

The correlations between  $W_{\text{HI}}$  and  $R$ , and those between  $W_{\text{HI}}$  and  $\tau_{353}$ , are shown in Figures 1 and 2, respectively, in which different colors represent different  $T_{\text{d}}$ . To match the resolution of the  $W_{\text{HI}}$  map, we smoothed the dust maps using a Gaussian kernel with a full width at half maximum (FWHM) of  $15''.4$ . In the northern region, we can confirm two trends of the dust–gas relation found by previous studies of the high-latitude sky described in Section 1: (1) we observe in Figure 1(a) a rather good correlation between  $W_{\text{HI}}$  and  $R$  over a wide range of  $T_{\text{d}}$ , as shown by [Planck Collaboration XI \(2014\)](#) that proposed  $R$  as a good neutral gas tracer,<sup>4</sup> and (2) we observe in Figure 1(b) a stronger  $T_{\text{d}}$  dependence of the  $W_{\text{HI}}-\tau_{353}$  relationship, which [Fukui et al. \(2015\)](#) interpreted as being primarily due to optically thick HI in low- $T_{\text{d}}$  areas. In the southern region, while both  $R$  and  $\tau_{353}$  show a small  $T_{\text{d}}$  dependence in the relation with  $W_{\text{HI}}$ , a possible non-linear relationship between  $W_{\text{HI}}$  and  $D_{\text{em}}$  (a break in the  $W_{\text{HI}}/D_{\text{em}}$  ratio) can be identified, particularly for the case of  $\tau_{353}$ .

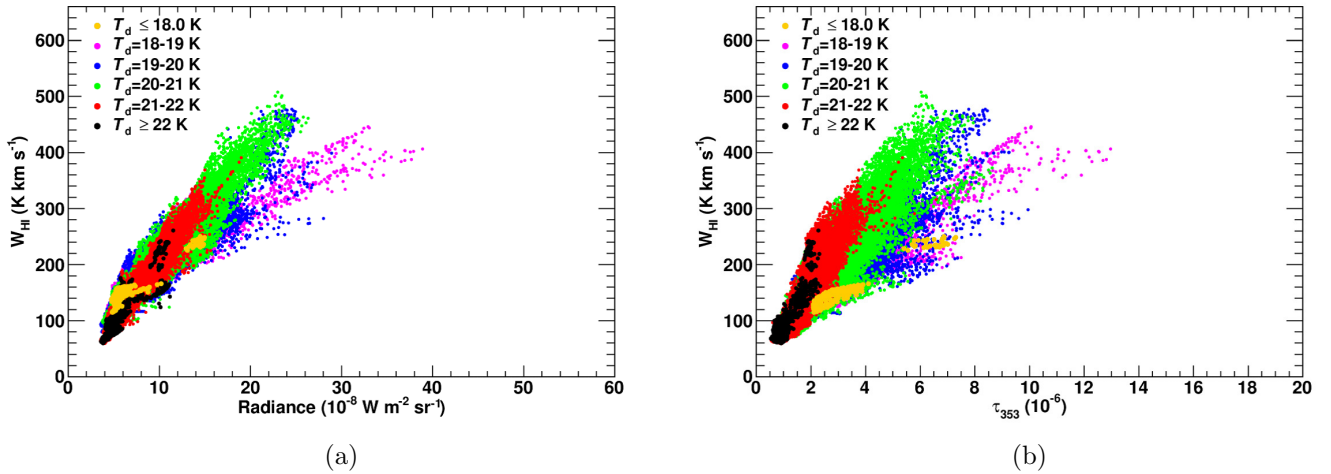


**Figure 1.** Correlations between  $W_{\text{HI}}$  and the dust tracers in the northern region. (a) Scatter plot of  $W_{\text{HI}}$  versus  $R$  and (b) scatter plot of  $W_{\text{HI}}$  versus  $\tau_{353}$ . In constructing these plots, the  $D_{\text{em}}$  ( $R$  and  $\tau_{353}$ ) maps were smoothed using a Gaussian kernel with the FWHM of  $15''.4$ . Each point represents one pixel in the underlying HEALPix map (order 9; with a mean spacing of  $6''.9$ ). The  $N_{\text{H}} \propto D_{\text{em}}$  relations calibrated using data in the high  $T_{\text{d}}$  area will be used to construct the initial  $N_{\text{H}}$  template maps in the  $\gamma$ -ray data analysis (see Section 2.2).

The correlation between the dust tracers and  $W_{\text{HI}}$  alone cannot distinguish which variable ( $R$  or  $\tau_{353}$ ) is the better tracer of the total dust and total gas column densities, and the correlation with the  $\gamma$ -ray intensity is crucial to reveal the true  $N_{\text{H}}$  distribution. Therefore, we prepared two types of  $N_{\text{H}}$  model maps based on  $R$  and  $\tau_{353}$ , in addition to the previously described  $N_{\text{H}}$  map based on  $W_{\text{HI}}$ , and tested them against the *Fermi*-LAT  $\gamma$ -ray data, in which the northern and southern regions were analyzed separately.

<sup>4</sup> They reported a good correlation up to column densities of (at least)  $5 \times 10^{20} \text{ cm}^{-2}$  (Figure 20 of the reference), which corresponds to a  $W_{\text{HI}}$  of  $\sim 280 \text{ K km s}^{-1}$ .

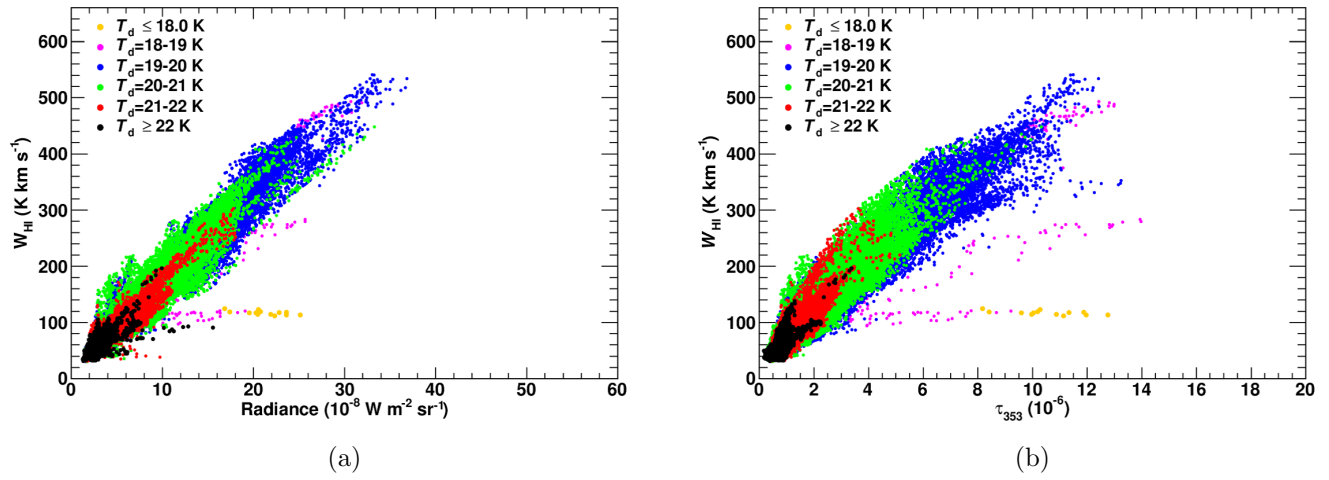


**Figure 2.** The same as Figure 1 but for the southern region.  $N_{\text{H}} \propto D_{\text{em}}$  relations calibrated using data in the high  $T_d$  and low  $W_{\text{HI}}$  area will be used to construct the initial  $N_{\text{H}}$  template maps in the  $\gamma$ -ray data analysis (see Section 2.2).

## 2.2. Construction of Gas Templates

We converted the  $W_{\text{HI}}$  map into an atomic hydrogen column density map by assuming the optically thin approximation ( $N_{\text{HI}}^{\text{thin}}(\text{cm}^{-2}) = 1.82 \times 10^{18} \cdot W_{\text{HI}}(\text{K km s}^{-1})$ ). The obtained  $N_{\text{HI}}^{\text{thin}}$  map and the  $T_{\text{d}}$  map in our ROI are shown in panels (a) and (b), respectively, in Figures 3 and 4. Under the assumption that all neutral gas is atomic and HI is optically thin, these  $N_{\text{HI}}^{\text{thin}}$  maps will be used as  $N_{\text{H}}$  template maps in the  $\gamma$ -ray data analysis (Section 3).

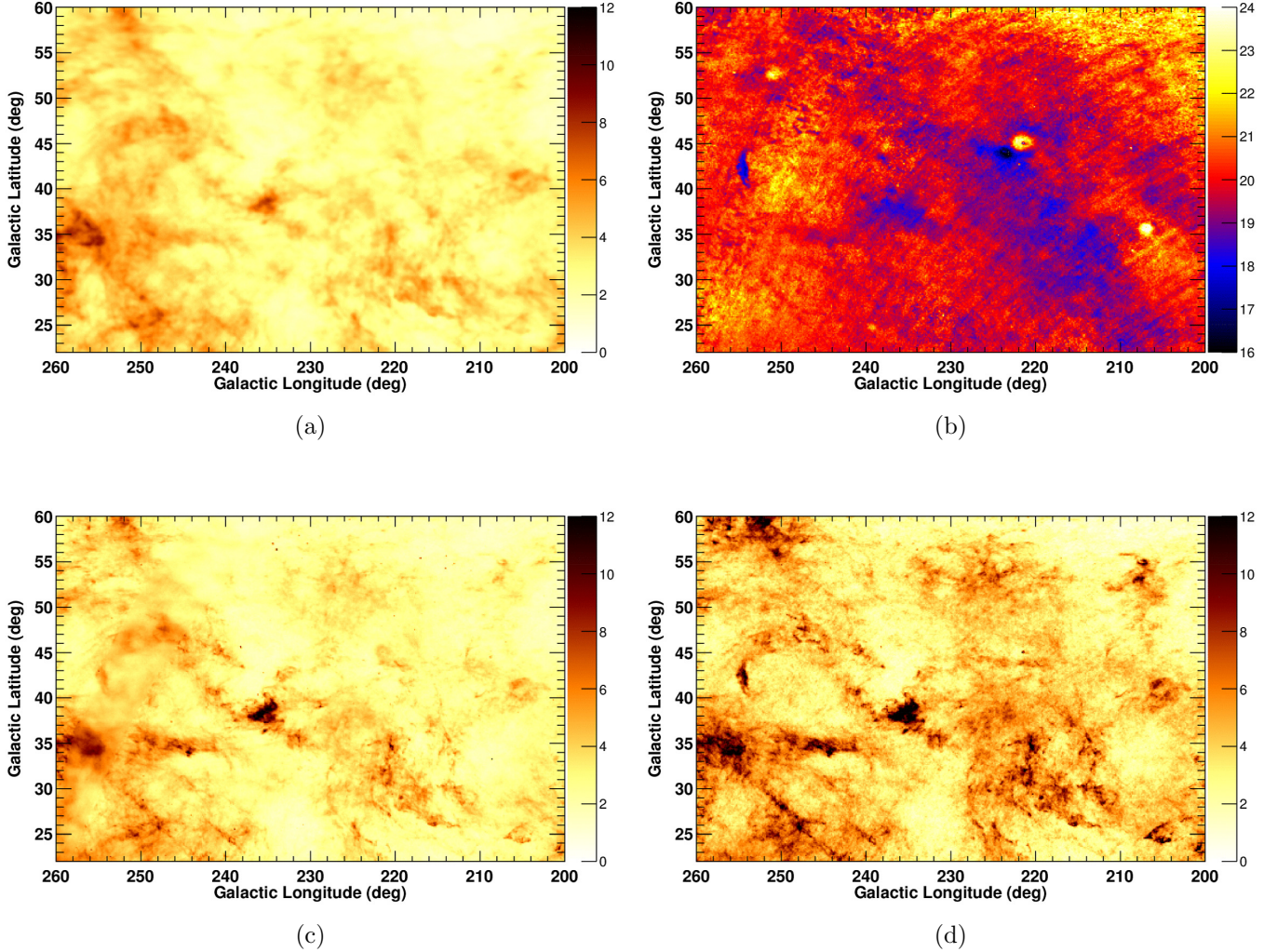


**Figure 3.** (a) The  $W_{\text{HI}}$  map converted to  $N_{\text{H}}$  under the assumption that all neutral gas is atomic and HI is optically thin ( $N_{\text{H}}(\text{cm}^{-2}) = 1.82 \times 10^{18} \cdot W_{\text{HI}}(\text{K km s}^{-1})$ ); (b) the  $T_{\text{d}}$  map (K); (c) the  $N_{\text{H}}$  template map proportional to  $R$  ( $N_{\text{H}}(\text{cm}^{-2}) = 38.4 \times 10^{26} \cdot R(\text{W m}^{-2} \text{ sr}^{-1})$ ); and (d) the  $N_{\text{H}}$  template map proportional to  $\tau_{353}$  ( $N_{\text{H}}(\text{cm}^{-2}) = 159 \times 10^{24} \cdot \tau_{353}$ ) for the northern region. The maps in panels (a), (c), and (d) are shown in units of  $10^{20} \text{ cm}^{-2}$ .



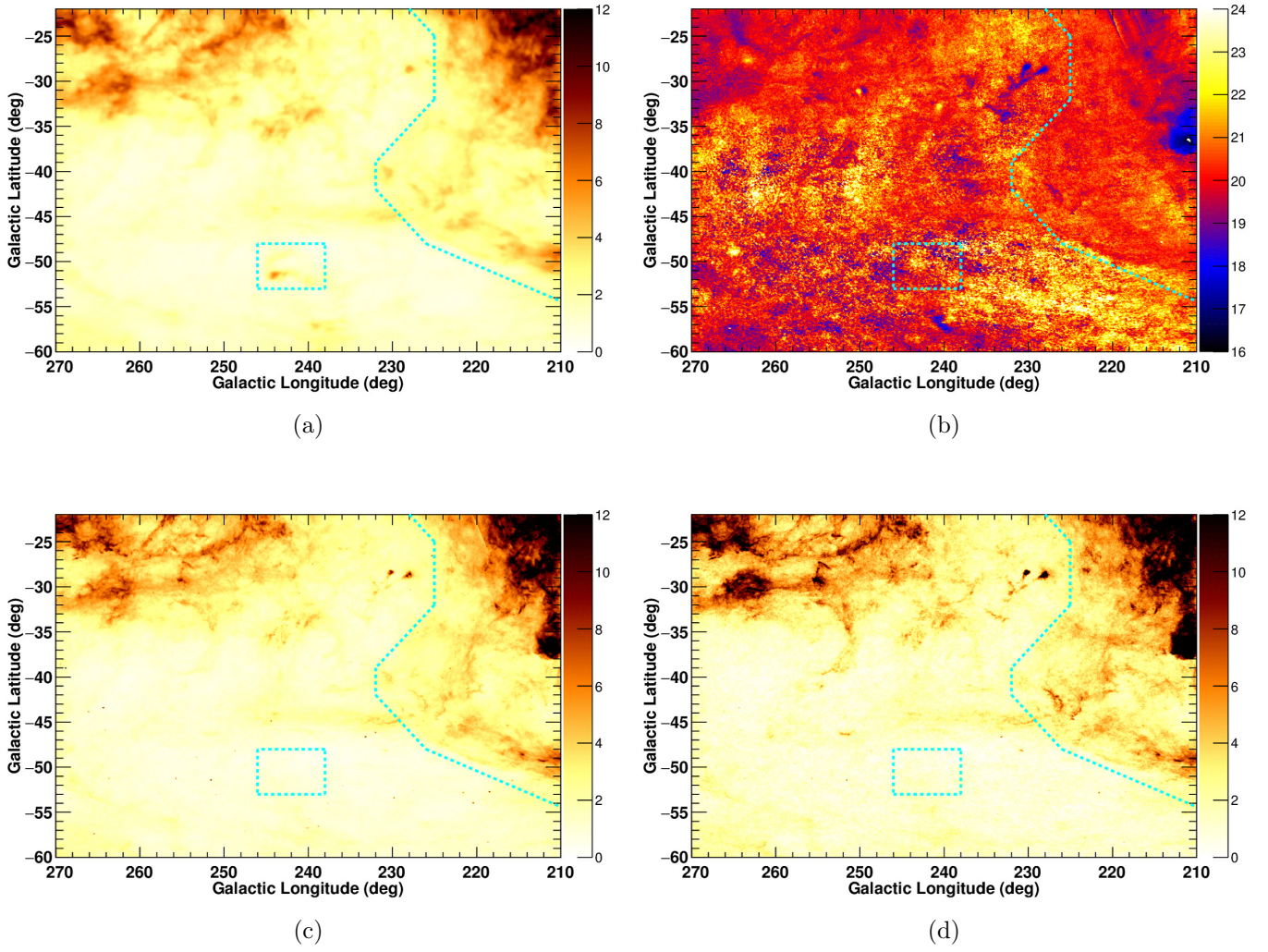


**Figure 4.** The same as Figure 3 but for the southern region. The region boundaries used for masking areas in the study of the  $W_{\text{HI}}-D_{\text{em}}$  relation and  $\gamma$ -ray data analysis are overlaid.  $N_{\text{H}}(\text{cm}^{-2}) = 32.0 \times 10^{26} \cdot R(W \text{ m}^{-2} \text{ sr}^{-1})$  and  $N_{\text{H}}(\text{cm}^{-2}) = 122 \times 10^{24} \cdot \tau_{353}$  are used in panels (c) and (d), respectively. One can see that areas of dense gas are away from the boundaries and therefore the spillover outside the masks is not severe.

To construct the  $N_{\text{H}}$  model maps based on the *Planck* dust models for the northern region, we assumed that  $N_{\text{H}}$  and  $D_{\text{em}}$  ( $R$  or  $\tau_{353}$ ) are proportional and that HI is optically thin, at least for the areas with high dust temperature ( $T_{\text{d}} \geq 21.0$  K). This assumption is based on the fact that high- $T_{\text{d}}$  areas show a  $\tau_{353}/W_{\text{HI}}$  ratio smaller than that in low- $T_{\text{d}}$  areas and are expected to have relatively high gas temperatures, and are therefore likely to be dominated by optically thin HI. The uniformity of the  $N_{\text{H}}/D_{\text{em}}$  ratio over the whole ROI will be tested in the  $\gamma$ -ray data analysis (Sections 4.1.2 and 4.2.2). First, we made a least-squares fit to the dust- $W_{\text{HI}}$  relationship for  $T_{\text{d}} \geq 21.0$  K in Figure 1 using a linear function with an intercept fixed at 0 because the zero-level of the dust emission is already subtracted in the *Planck* dust models (Planck Collaboration XI 2014). We obtained coefficients of  $21.1 \times 10^8 \text{ K km s}^{-1} (W \text{ m}^{-2} \text{ sr}^{-1})^{-1}$  and  $87.2 \times 10^6 \text{ K km s}^{-1}$  for  $R$  and  $\tau_{353}$ , respectively. In these fits,  $W_{\text{HI}}$  is treated as an independent variable because the signal-to-noise ratio

is much greater than that of  $D_{\text{em}}$ . Then, we converted  $R$  (or  $\tau_{353}$ ) into  $N_{\text{H}}$  maps using the obtained coefficients and multiplied by  $1.82 \times 10^{18} \text{ cm}^{-2} (\text{K km s}^{-1})^{-1}$ . This gives a conversion factor for  $R$  of  $38.4 \times 10^{26} \text{ cm}^{-2} (\text{W m}^{-2} \text{ sr}^{-1})^{-1}$ , and for  $\tau_{353}$  of  $159 \times 10^{24} \text{ cm}^{-2}$ . The obtained  $N_{\text{H}}$  template maps are shown in Figure 3 (panels (c) and (d), respectively). By comparing these  $N_{\text{H}}$  model maps we can see that the map based on  $W_{\text{HI}}$  shows the weakest contrast. The  $\tau_{353}$ -based map predicts the strongest contrast and approximately a factor of 2 higher  $N_{\text{H}}$  in the dense clouds compared to the  $W_{\text{HI}}$ -based map, while the  $R$ -based map shows a moderate contrast. Thus, they will give different contrasts in the predicted  $\gamma$ -ray map and can be tested by the fit quality to the  $\gamma$ -ray data (Section 4).

For the southern region, we also assumed that  $W_{\text{HI}}$  and  $D_{\text{em}}$  are proportional and followed the same procedure as that for the northern region. The obtained coefficients for the dust- $W_{\text{HI}}$  relationship are  $17.6 \times 10^8 \text{ K km s}^{-1} (\text{W m}^{-2} \text{ sr}^{-1})^{-1}$  and  $66.9 \times 10^6 \text{ K km s}^{-1}$ , and the conversion factors to construct  $N_{\text{H}}$  model are  $32.0 \times 10^{26} \text{ cm}^{-2} (\text{W m}^{-2} \text{ sr}^{-1})^{-1}$  and  $122 \times 10^{24} \text{ cm}^{-2}$  for  $R$  and  $\tau_{353}$ , respectively. The obtained  $N_{\text{H}}$  template maps are shown in Figure 4; the contrast of the gas density is weakest for the map based on  $W_{\text{HI}}$ , while that based on  $\tau_{353}$  is the strongest.

Another possible source of diffuse  $\gamma$ -ray emissions is CR interactions with ionized gas. To estimate this contribution, we referred to Casandjian (2015) and used the free-free intensity map at a frequency of 22.7 GHz extracted from nine years of *WMAP* observations, namely `wmap_K_mem_freefree_9yr_v5.fits` (Bennett et al. 2013), as a template for the  $\gamma$ -ray emission correlated with the ionized hydrogen (H II). We used the scaling factor adopted by Casandjian (2015),  $1.3 \times 10^{20} \text{ cm}^{-2} \text{ mK}^{-1}$ , and constructed an H II column density ( $N_{\text{HII}}$ ) model map. We confirmed that the average column density is only a few % of the neutral gas column density estimated by  $W_{\text{HI}}$  shown in Figure 3(a) and 4(a). Therefore the contribution of the ionized gas to  $\gamma$ -ray emission is small, and the  $N_{\text{HII}}$ -related term will be fixed in the  $\gamma$ -ray data analysis (Section 3).

### 3. GAMMA-RAY DATA AND MODELING

#### 3.1. *Gamma-ray Observations and Data Selection*

The LAT on board the *Fermi Gamma-ray Space Telescope*, launched in June 2008, is a pair-tracking  $\gamma$ -ray telescope, detecting photons in the energy range from  $\sim 20$  MeV to more than 300 GeV. Details of the LAT instrument and the pre-launch performance expectations can be found in [Atwood et al. \(2009\)](#), and the on-orbit calibration is described in [Abdo et al. \(2009a\)](#). Past studies of the Galactic diffuse emissions by *Fermi*-LAT can be found in, e.g., [Ackermann et al. \(2012a\)](#), and [Casandjian \(2015\)](#).

Routine science operations with the LAT started on August 4, 2008. We used a data taking interval from August 4, 2008 to August 1, 2016 (i.e., eight years), to study diffuse  $\gamma$ -rays in our ROI ( $200^\circ \leq l \leq 260^\circ$  and  $210^\circ \leq l \leq 270^\circ$  for the northern and southern regions, respectively, with  $22^\circ \leq |b| \leq 60^\circ$  for both). During most of this time, the LAT was operated in sky survey mode, obtaining complete sky coverage every two orbits (which corresponds to  $\sim 3$  h) and a relatively uniform exposure. Because the diffuse  $\gamma$ -ray emission from the ISM is greatly extended and the intensity is rather weak at high latitudes, having a clean (low background) sample of photons is crucial. Therefore, we used the latest release of the Pass 8 data (P8R3) recently made public by the LAT collaboration. The previous data set (P8R2) is known to suffer from a residual background with a peak along the ecliptic plane which is inside our ROI in the northern region. We used the standard LAT analysis software, *Fermi* Science Tools <sup>5</sup> version v10r00p05 to select events above 100 MeV <sup>6</sup> because good angular resolution is essential for examining the correlation between  $\gamma$ -rays and gas distribution, and selected events of the SOURCE class. The instrument response function (IRF) that matches our data set and event selection, P8R3\_SOURCE\_V2, was used in the following analysis. We also analyzed data using the cleanest ULTRACLEANVETO class and corresponding IRF and found that a decrease of the isotropic component (see Section 3.2), which includes the residual background, was marginal (within  $\leq 10\%$ ). Therefore, we keep using the SOURCE class to maximize the photon statistics. In addition, we required that the reconstructed zenith angles of the arrival direction of the photons be less than  $100^\circ$  and  $90^\circ$  for energies above and below 200 MeV, respectively, to reduce contamination by photons from Earth's atmosphere. To accommodate the rather poor angular resolution at low energy, below 200 MeV, we used events and the responses of point-spread function (PSF) event types 2 and 3; meanwhile, above 200 MeV, we did not apply selections based on PSF event types and used events and the responses of Front + Back. As described in Section 3.3, we carried out a bin-by-bin likelihood fitting, and data below and above 200 MeV are analyzed separately. We stopped at 25.6 GeV because of poor photon statistics above that energy. We used `gtselect` command to apply the selections described above.

In addition, we excluded periods of time during which the LAT detected bright  $\gamma$ -ray bursts or solar flares (by using `gtmktime` command); the integrated period of time excluded in this procedure was negligible (less than 1%) compared to the total observation time. The data count maps in the northern and southern regions of our ROI are given in Figure 5.

<sup>5</sup> <http://fermi.gsfc.nasa.gov/ssc/data/analysis/software/>

<sup>6</sup> In Section 4.2.1, we also used data below 100 MeV as a preparatory stage of the analysis in order to dissolve a coupling among fit components.



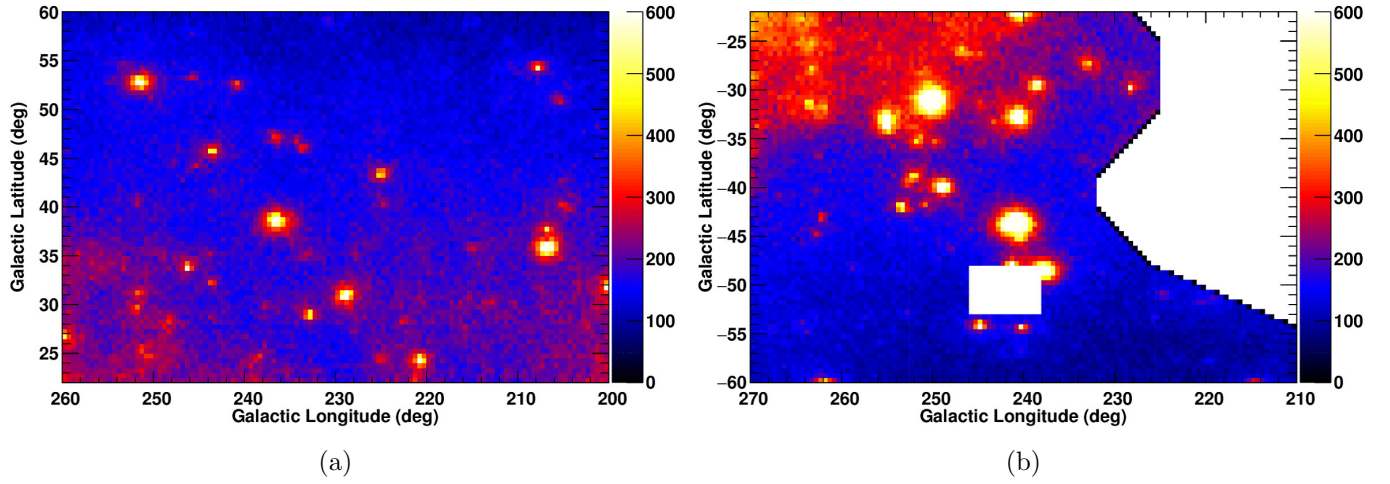


**Figure 5.** *Fermi*-LAT  $\gamma$ -ray count maps ( $E \geq 100$  MeV) of the regions we analyzed. The maps are in a Cartesian projection, and the northern and southern regions are shown in panels (a) and (b), respectively. Although the fit has been performed in  $0^\circ.25 \times 0^\circ.25$  bins above 400 MeV, all the data have been re-binned in  $0^\circ.5 \times 0^\circ.5$  pixels for display.

### 3.2. Model to Represent the Gamma-ray Emission

We modeled the  $\gamma$ -ray emission above 100 MeV observed by *Fermi*-LAT as a linear combination of the  $N_{\text{H}}$  model map constructed from the HI4PI survey data ( $W_{\text{HI}}$ ) or the *Planck* dust map ( $R$  or  $\tau_{353}$ ) (see Section 2.2), the template map for  $N_{\text{HII}}$ , the IC emission, the isotropic component, the emission from the Sun and Moon (e.g. [Abdo et al. 2011](#); [Ackermann et al. 2016](#)), and the  $\gamma$ -ray point sources. The use of the gas column density map as a template is based on the assumption that  $\gamma$ -rays are generated via interactions between CRs and the ISM gas and that the CR intensity does not vary significantly over the scale of the interstellar complexes in this study. This assumption is simple but very plausible, particularly in high-latitude regions (where most of the gas is expected to be local), such as the one studied here. We started with a single  $N_{\text{H}}$  map (in Sections 4.1.1 and 4.2.1) and then tested multiple  $N_{\text{H}}$  maps based on the *Planck* dust model maps (in Sections 4.1.2 and 4.2.2). To model the  $\gamma$ -rays produced via IC scattering, we used GALPROP <sup>7</sup> (e.g., [Strong & Moskalenko 1998](#); [Strong et al. 2007](#)), a numerical code that solves the CR transport equation within the Galaxy and predicts the  $\gamma$ -ray emission produced via the interactions of CRs with interstellar gas and low-energy photons. The IC emission is calculated from the distribution of the propagated electrons and the interstellar radiation field developed by [Porter et al. \(2008\)](#). Here, we adopted the IC model map produced in the GALPROP run 54\_Yusifov\_z4kpc\_R30kpc\_Ts150K\_EBV2mag,<sup>8</sup> which was developed by [Ackermann et al. \(2012a\)](#) and has been used in other LAT collaboration publications<sup>9</sup> such as [Planck Collaboration Int. XXVIII \(2015\)](#), and [Remy et al. \(2017\)](#). To model individual  $\gamma$ -ray sources, we referred to the preliminary *Fermi*-LAT eight-year point source list (FL8Y),<sup>10</sup> which is based on the first eight years of the science phase of the mission and includes more than 5000 sources detected at a significance of  $\geq 4\sigma$ . We note that the list is built using the same lowest energy threshold (0.1 GeV) as the present study. For our analysis, we considered 151 and 142 FL8Y sources (detected at a significance of  $\geq 4\sigma$ ) in the northern and southern regions, respectively, and 27 bright sources just outside the ROIs ( $\geq 50\sigma$  within  $10^\circ$  and  $\geq 20\sigma$  within  $1^\circ$ ) to take into account possible contaminations from their emission caused by overlap because of the breadth of the PSF. We modeled a (quasi-) isotropic component to represent the contributions to our ROI due to extragalactic diffuse emission and the residual instrumental background from misclassified CR interactions in the LAT detector by the uniform emission in our ROI. A template of the ionized gas was constructed based on the *WMAP* free-free intensity map as described in Section 2.2. We included the templates for the  $\gamma$ -ray emission from the Sun and Moon that were used in the initial sky models for the fourth LAT source catalog (4FGL) ([Abdollahi et al. 2019](#)), which is based on the first eight years of LAT observations. Specifically, we used template\_SunDiskMoonv3r2\_8years\_zmax105.fits and template\_SUNICv2.8years\_zmax105.fits.<sup>11</sup>

Then, the  $\gamma$ -ray intensity  $I_\gamma(l, b, E)$  (ph s<sup>-1</sup> cm<sup>-2</sup> sr<sup>-1</sup> MeV<sup>-1</sup>) can be modeled as

$$I_\gamma(l, b, E) = q_\gamma(E) [c_1(E) \cdot N_{\text{H}}(l, b) + N_{\text{HII}}(l, b)] + c_2(E) \cdot I_{\text{IC}}(l, b, E) \\ + I_{\text{iso}}(E) + c_3(E) \cdot I_{\text{SM}}(l, b, E) + \sum_j P_j(l, b, E) \quad , \quad (1)$$

<sup>7</sup> <http://galprop.stanford.edu>

<sup>8</sup> The file is available at <https://galprop.stanford.edu/PaperIISuppMaterial/>

<sup>9</sup> <https://www-glast.stanford.edu/cgi-bin/pubpub>

<sup>10</sup> <https://fermi.gsfc.nasa.gov/ssc/data/access/lat/fl8y/>

<sup>11</sup> These files will be made available at [http://www-glast.stanford.edu/pub\\_data](http://www-glast.stanford.edu/pub_data)

where  $N_{\text{H}}(l, b)$  is the total neutral gas column density model (based on  $W_{\text{HI}}$ ,  $R$ , or  $\tau_{353}$ ) in  $\text{cm}^{-2}$ ,  $N_{\text{HII}}(l, b)$  is the gas column density model from ionized gas in  $\text{cm}^{-2}$ ,  $q_{\gamma}(E)$  ( $\text{ph s}^{-1} \text{sr}^{-1} \text{MeV}^{-1}$ ) is the model of the differential  $\gamma$ -ray yield or  $\gamma$ -ray emissivity per H atom,  $I_{\text{IC}}(l, b, E)$ ,  $I_{\text{iso}}(E)$ , and  $I_{\text{SM}}(l, b, E)$  are the IC model, (quasi-)isotropic background intensities, and model of the emission from the Sun and Moon (each in units of  $\text{ph s}^{-1} \text{cm}^{-2} \text{sr}^{-1} \text{MeV}^{-1}$ ), respectively, and  $P_j(l, b, E)$  represents the point source contributions. We used the  $\gamma$ -ray emissivity model  $q_{\gamma}(E)$  of the local interstellar spectrum (LIS) of the CRS (protons and electrons) adopted in [Abdo et al. \(2009b\)](#), specifically the model curve for the nuclear enhancement factor  $\epsilon_{\text{M}}$  (a scale factor to take into account the effect of heavy nuclei in both CRS and the target matter) of 1.84 ([Mori 2009](#)). In other words,  $q_{\gamma}(E)$  is decomposed as  $1.84 \cdot q_{\gamma}(\text{pp}) + q_{\gamma}(\text{brems})$  where  $q_{\gamma}(\text{pp})$  and  $q_{\gamma}(\text{brems})$  are the  $\gamma$ -ray emissivity models due to the proton–proton interaction and electron bremsstrahlung, respectively. To accommodate the uncertainties in the LIS and  $\epsilon_{\text{M}}$ , we included a scale factor ( $c_1(E)$  in Equation (1)) as a free parameter. This parameter is 1.0 if the measured  $\gamma$ -ray emissivity agrees with the LIS and  $\epsilon_{\text{M}}$  we adopted. Because the estimated ionized gas column density is small (at the maximum  $\sim 1 \times 10^{20} \text{cm}^{-2}$ ), we fixed the scale factor at 1.0 for the  $N_{\text{HII}}(l, b)$  template to obtain a stable fitting. The IC emission model is also uncertain, and we included another scale factor ( $c_2(E)$  in Equation (1)) as a free parameter. The extragalactic diffuse emission and the residual background are modeled by the isotropic term,  $I_{\text{iso}}$ , as a uniform template. The intensity of this component could exhibit large-scale fluctuations due to the uncertainty of the LAT response and/or possible non-uniformity of the background. Therefore we include the isotropic term in each energy band rather than adopt the template provided by the LAT collaboration<sup>12</sup> nor determine it by the fit outside of our ROI. We note that the isotropic term is a dominant component (see Section 4); therefore we should be able to constrain its contribution using the data in our ROI. The scale factor for  $I_{\text{SM}}(l, b, E)$ ,  $c_3(E)$ , was taken to be a free parameter in the northern region where the ecliptic circle goes through our ROI, even though it was fixed to 1.0 in the southern region. The point source contributions were also taken to be free parameters as a function of energy. The positions of the sources were fixed to the values in FL8Y. To model the contamination from outside the ROI, we used the  $N_{\text{H}}$ ,  $I_{\text{IC}}$ , and  $I_{\text{SM}}$  maps including peripheral regions.

Among the model components described above, the  $\gamma$ -ray emission model from Sun and Moon was adopted from the work for the 4FGL while it was in the development phase. The model will be outdated when the work to construct the 4FGL is complete. However, we confirmed that the choice of the Sun and Moon template does not affect the fit for the neutral gas component as described in Sections 4.1.1 and 4.1.2. Because the IC model has uncertainty, we also examined the effect as described in Sections 4.1.2 and 4.2.2.

### 3.3. Model Fitting Procedure

We divided the  $\gamma$ -ray data from 0.1 to 25.6 GeV into eight energy ranges using logarithmically equally spaced energy bands, and each band was divided into four sub bins. Then, we fit Equation (1) to data in each energy band in  $0.5 \times 0.5$  bins below 400 MeV (where the PSF (68% contaminant radius) is  $\geq 2^\circ$ ) and  $0.25 \times 0.25$  bins above 400 MeV using the binned maximum-likelihood method with Poisson statistics implemented in the Science Tools. In each narrow energy band,  $c_1$ ,  $c_2$ , and  $c_3$  were modeled as energy-independent normalization factors. Because  $I_{\text{iso}}(E)$  is the most dominant

<sup>12</sup> <https://fermi.gsfc.nasa.gov/ssc/data/access/lat/BackgroundModels.html>

component over the entire energy range, it was modeled via a power-law function with both photon index and normalization as free parameters in each energy band.  $P_j(l, b, E)$  were modeled via separate power-law functions in each energy band with only the normalization allowed to vary; the photon index was fixed at 2.2 as a representative value of the high-latitude LAT sources (FSRQ and BL Lac; [Ackermann et al. 2015](#)).

When modeling the point sources, we iteratively included them in several groups at a time in order of decreasing significance. First, we included and fitted the brightest sources detected in FL8Y at more than  $35\sigma$ ; then, we added and fit a second group detected at  $20\text{--}35\sigma$ , freezing the already included source parameters. In this way, we worked down to the sources detected at more than  $4\sigma$  in FL8Y. For each step, the parameters of the diffuse emission model ( $c_1$ ,  $c_2$ ,  $c_3$ , and  $I_{\text{iso}}$ ) were always left free to vary. After we reached the least-significant sources (more than  $4\sigma$ ) we went back to the brightest ones (more than  $35\sigma$  significance), and let them and diffuse emission models free to vary while parameters of other sources are kept fixed to those already determined. We repeated the process until the increment of the log-likelihoods,  $\ln L$ <sup>13</sup>, was less than 0.1 over one loop in each energy band. To model the contamination from outside the ROI, we took into account sources (with the model parameters fixed to those of FL8Y) detected above  $50\sigma$  located at a distance  $\leq 10^\circ$  from the region boundaries, or detected above  $20\sigma$  and located within  $\leq 1^\circ$  from the boundaries. Other sources outside of our ROIs are not considered.

<sup>13</sup>  $L$  is conventionally calculated as  $\ln L = \sum_i n_i \ln(\theta_i) - \sum_i \theta_i$ , where  $n_i$  and  $\theta_i$  are the data and the model-predicted counts in each pixel (for each energy band) denoted by the subscript, respectively (see, e.g., [Mattox et al. 1996](#)).

## 4. GAMMA-RAY DATA ANALYSIS

## 4.1. Northern Region

## 4.1.1. Initial Modeling with a Single Gas Map

First, we analyzed the northern region and started our data analysis using individual  $N_{\text{H}}$  model maps based on the HI4PI survey data or the *Planck* dust model maps described in Section 2.2: We used  $N_{\text{H}}(\text{cm}^{-2}) = 1.82 \times 10^{18} \cdot W_{\text{HI}}(\text{K km s}^{-1})$ , or  $N_{\text{H}}(\text{cm}^{-2}) = 38.4 \times 10^{26} \cdot R(\text{W m}^{-2} \text{sr}^{-1})$ , or  $N_{\text{H}}(\text{cm}^{-2}) = 159 \times 10^{24} \cdot \tau_{353}$ .

We fit the  $\gamma$ -ray data as described in Section 3.3;  $c_1$ ,  $c_2$ ,  $c_3$ ,  $I_{\text{iso}}$ , and  $P_j$  are free parameters in each energy band. As described in Section 3.3, point sources are included iteratively. We remind the reader that the dust-based templates are equivalent to  $N_{\text{H}} = \left( \overline{N_{\text{HI}}^{\text{thin}}/D_{\text{em}}} \right) \cdot D_{\text{em}}$  where  $\overline{N_{\text{HI}}^{\text{thin}}/D_{\text{em}}}$  is the average of the  $N_{\text{HI}}^{\text{thin}}/D_{\text{em}}$  ratio calibrated in the high- $T_{\text{d}}$  regions. Therefore, in this initial modeling, we implicitly assume that the  $N_{\text{H}}/D_{\text{em}}$  ratio is constant over the whole  $T_{\text{d}}$  range.

The obtained values of  $\ln L$ , summed over the entire energy range with the  $R$ -based and  $\tau_{353}$ -based  $N_{\text{H}}$  maps are 62.2 and -455.5, respectively, when compared to that of the  $W_{\text{HI}}$ -based  $N_{\text{H}}$  map. Therefore, the  $R$ -based  $N_{\text{H}}$  map is preferred by the  $\gamma$ -ray data and the  $\tau_{353}$ -based map is disfavored. This conclusion is unchanged even if we do not include weak sources (detected at less than  $5\sigma$ ), or if we change the energy threshold higher (200 or 400 MeV) to reduce the coupling with sources. By looking at the residual maps summarized in Figure 6, we can identify extended positive residuals covering the range of  $l$  in  $245\text{--}260^\circ$  and  $b$  in  $30\text{--}55^\circ$  in the  $\tau_{353}$ -based map which makes the  $\ln L$  significantly worse. Although the difference of the  $\ln L$  values is smaller between  $W_{\text{HI}}$ -based analysis and  $R$ -based ones, we can also identify positive residuals in the  $W_{\text{HI}}$ -based map at around  $(l, b) = (259^\circ, 24^\circ)$ ,  $(256^\circ, 33^\circ.5)$ , and  $(236^\circ, 37^\circ.5)$ , which corresponds to a coherent low- $T_{\text{d}}$  and high- $W_{\text{HI}}$  (and  $D_{\text{em}}$ ) area. These are the areas where the  $W_{\text{HI}}$ -based  $N_{\text{H}}$  map predicts smaller gas column density. We note that a region of apparently flat residuals at  $(l, b) \sim (236^\circ.5, 38^\circ.5)$  (where a difference of predicted  $N_{\text{H}}$  is the largest) is visible in all the three analyses, even though the predicted  $N_{\text{H}}$  is rather different there. This is likely due to the interplay with a weak ( $\leq 8\sigma$ )  $\gamma$ -ray source FL8Y J0946.2+0104 located at  $(l, b) \sim (235^\circ.37, 38^\circ.56)$ . The averages of the normalizations (weighted inversely by the square of the error in each band) for the neutral gas component,  $c_1$  in Equation (1), are  $1.028 \pm 0.011$ ,  $0.964 \pm 0.012$ , and  $0.615 \pm 0.008$  for the  $W_{\text{HI}}$ -based,  $R$ -based, and  $\tau_{353}$ -based maps, respectively.

The emission from the Sun and the Moon is subdominant in the region, but it could still have a small effect on the results. To test this effect, we redid the analysis with the model of the Sun and Moon emission used for the LAT 3FGL catalog (Acero et al. 2015). The change in the scale factors of the  $N_{\text{H}}$  map is negligible ( $\leq 1\%$ ) and the results are thus not affected by this component.

We also note that the normalization of the IC term ( $c_2(E)$  in Equation (1)) is nearly 0 for the  $R$ -based analysis, likely (at least partially) because of the interplay with the isotropic term (the dominant component<sup>14</sup> in our ROI). Because the data prefer the fit with  $c_2(E) \sim 0$ , we maintain the results but will examine the systematic uncertainty by employing alternative IC models and fixing  $c_2(E)$  to 1.0 (Sections 4.1.2 and 5.2).

<sup>14</sup> We note that fixing the IC normalization to 1 gives the IC flux to be only 1/5 of the isotropic component.



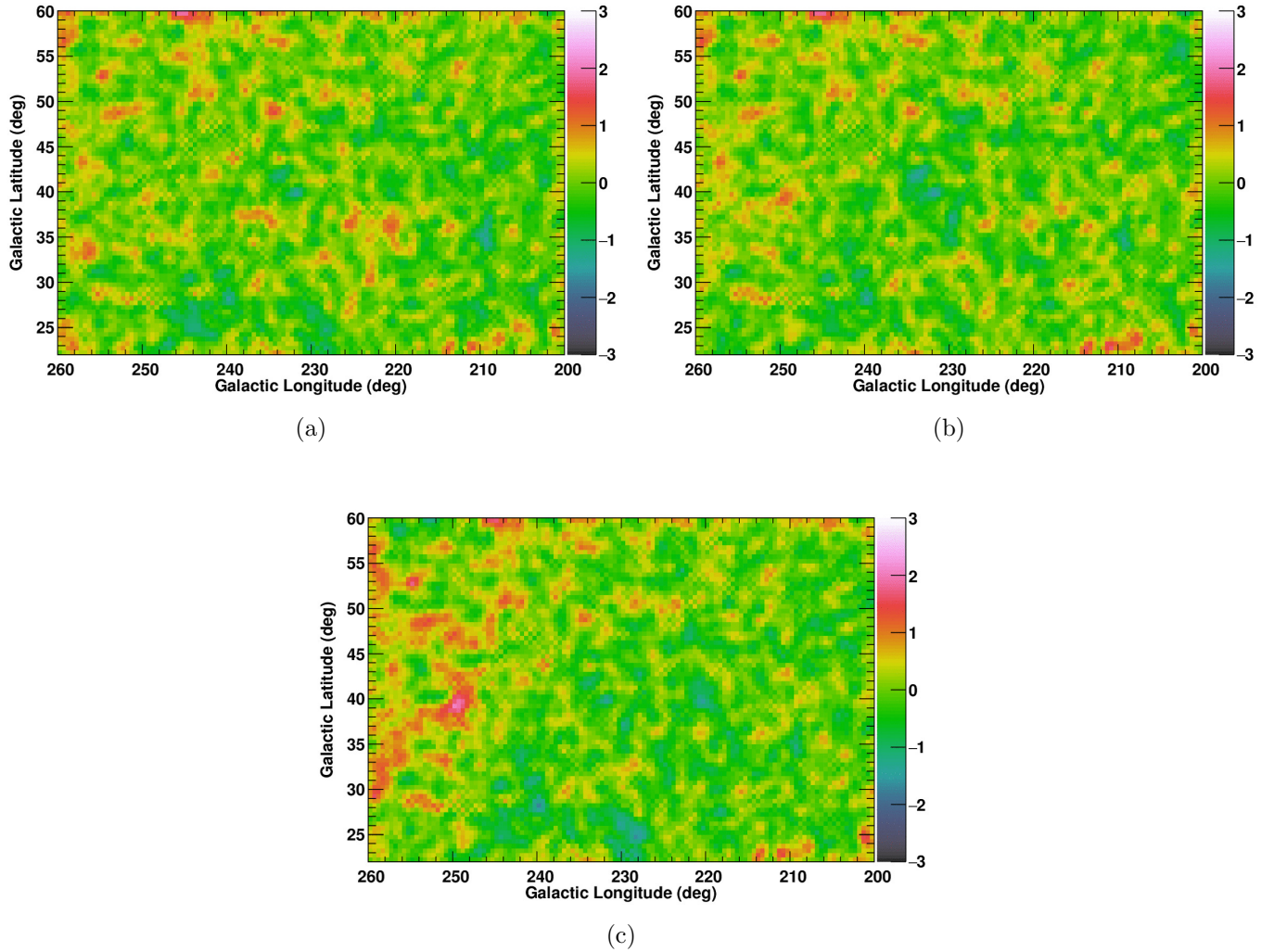


**Figure 6.** The residual maps (in units of sigma) obtained from the fit with the  $N_H$  model template based on (a)  $W_{H1}$ , (b)  $R$ , and (c)  $\tau_{353}$ . Although the fit has been performed in  $0^\circ.25 \times 0^\circ.25$  bins above 400 MeV, all the data have been re-binned in  $0^\circ.5 \times 0^\circ.5$  pixels for display and smoothed with a k3a kernel (1-2-1 two-dimensional boxcar smoothing) in the ROOT framework (<https://root.cern.ch>).



4.1.2. *Dust Temperature-Sorted Modeling*

As we saw in Section 2.1 (Figure 1), the correlation between  $W_{\text{HI}}$  and  $D_{\text{em}}$  depends on  $T_{\text{d}}$ , and the temperature dependence is significantly different in the cases of  $R$  or  $\tau_{353}$ . Although the model with  $N_{\text{H}}$  proportional to  $R$  is preferred to the one proportional to  $\tau_{353}$  (and the one proportional to  $W_{\text{HI}}$ ) in terms of  $\ln L$  by the  $\gamma$ -ray data analysis as described in Section 4.1, the true  $N_{\text{H}}$  distribution could be appreciably different from either of them; see Section 2.1 for the prerequisites for  $D_{\text{em}}$  to be proportional to  $N_{\text{H}}$  and also Mizuno et al. (2016), who reported the apparent  $T_{\text{d}}$  dependence of  $N_{\text{H}}/R$  and  $N_{\text{H}}/\tau_{353}$  in the MBM 53, 54, and 55 clouds and the Pegasus loop.

Therefore, we performed an analysis with the  $T_{\text{d}}$ -sorted  $N_{\text{H}}$  template maps. We split the  $N_{\text{H}}$  template map (constructed from  $R$  or  $\tau_{353}$ ) into four templates based on  $T_{\text{d}}$ , for  $T_{\text{d}} \leq 19$  K,  $T_{\text{d}} = 19\text{--}20$  K,  $T_{\text{d}} = 20\text{--}21$  K, and  $T_{\text{d}} \geq 21$  K<sup>15</sup>, and fit the  $\gamma$ -ray data with Equation (1) but using  $\sum_i c_{1,i}(E) \cdot N_{\text{H},i}(l, b)$  instead of  $c_1(E) \cdot N_{\text{H}}(l, b)$ , where  $c_{1,i}(E)$  and  $N_{\text{H},i}(l, b)$  represent the scale factor and the template gas map for each of the four templates. Under the assumption of a uniform CR intensity,  $c_{1,i}(E)$  should not show  $T_{\text{d}}$  dependence if the  $N_{\text{H}}/D_{\text{em}}$  ratio is constant. To keep the fit stable while accommodating more free parameters, in this analysis (and that in Section 4.2.2) we omitted the lowest-energy band (where the angular resolution is poor) and the highest energy band (where the photon statistics is low) so that the energy bands are restricted to the range 0.2–12.8 GeV. The improvement in the fits, the likelihood test statistics  $\text{TS} \equiv 2\Delta \ln L$ , were 41.4 and 496.6 with 18 more degrees of freedom (giving statistical significances of  $3.2\sigma$  and  $20\sigma$ ) for the  $R$ -based and  $\tau_{353}$ -based fit, respectively. Therefore, the fit improvement was significant in both cases<sup>16</sup>; however the  $R$ -based analysis was still preferred.

Tables 1 and 2 show how the scaling factor  $c_{1,i}(E)$  depends on  $T_{\text{d}}$ , and the averages over 0.2–12.8 GeV are summarized in Figure 7. The  $\tau_{353}$ -based analysis reveals a positive correlation (a lower scaling factor in  $T_{\text{d}} \leq 20$  K), implying an overestimation of  $N_{\text{H}}/\tau_{353}$  in the low  $T_{\text{d}}$  area. Even though a negative correlation might be seen in the  $R$ -based analysis, the dependence on  $T_{\text{d}}$  is less clear and the fit improvement over the analysis with the single  $N_{\text{H}}$  template map is moderate. Therefore careful examination of the systematic uncertainties is required.

A possible systematic effect that might affect the  $T_{\text{d}}$  dependence is the uncertainty of the IC model. Even if we adjust the IC spectrum by scaling it in each energy range, the spatial distribution of our IC model might not be accurate. This could affect the results shown in Figure 7 in two ways; by changing the  $T_{\text{d}}$  dependence of the scaling factor (i.e., the measured  $T_{\text{d}}$  dependence of  $N_{\text{H}}/D_{\text{em}}$ ) and by changing the values of the scaling factor (i.e., the measured  $\gamma$ -ray emissivity or CR intensity). If there is a small spatial variation of the (quasi-)isotropic component that is dominant in our ROI, and this uncertainty is not absorbed by the IC model, the scale factors of the  $N_{\text{H}}$  templates will be affected as well. In order to investigate such possibilities, we tested several alternative IC models. As described in Section 3.2, we used the IC model produced in the GALPROP run 54\_Yusifov\_z4kpc\_R30kpc\_Ts150K\_EBV2mag as our baseline model. This configuration assumes a CR source distribution proportional to the pulsar distribution of Yusifov & Kücük (2004) and a CR halo size  $z_h$  of 4 kpc. As described in Ackermann et al. (2011), de Palma et al. (2012), and Ackermann et al. (2012a), the CR source

<sup>15</sup> For information, the relative values of the integral of  $R \times$  solid angle are 7.1%, 44.8%, 41.4%, and 7.0% for  $T_{\text{d}} \leq 19$  K,  $T_{\text{d}} = 19\text{--}20$  K,  $T_{\text{d}} = 20\text{--}21$  K, and  $T_{\text{d}} \geq 21$  K, respectively, and those of  $\tau_{353} \times$  solid angle are 8.5%, 47.4%, 38.6%, and 5.5% for  $T_{\text{d}} \leq 19$  K,  $T_{\text{d}} = 19\text{--}20$  K,  $T_{\text{d}} = 20\text{--}21$  K, and  $T_{\text{d}} \geq 21$  K, respectively. They give the relative contribution to the  $\gamma$ -ray flux under the assumption of uniform CR intensity.

<sup>16</sup> TS with respect to the null hypothesis is asymptotically distributed as a chi-square with the degrees of freedom equal to the difference in the number of free parameters between two hypotheses ([http://fermi.gsfc.nasa.gov/ssc/data/analysis/documentation/Cicerone/Cicerone\\_Likelihood/Likelihood\\_overview.html](http://fermi.gsfc.nasa.gov/ssc/data/analysis/documentation/Cicerone/Cicerone_Likelihood/Likelihood_overview.html)).

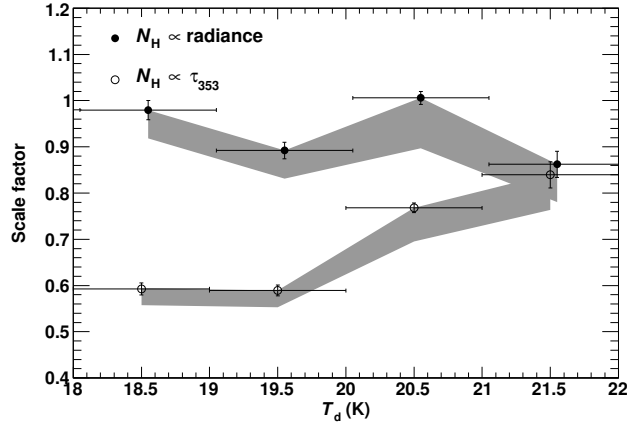


**Figure 7.** Summary of the scale factors  $c_{1,i}$  in Equation (1) averaged over 0.2–12.8 GeV in each range of  $T_d$ . The filled and open circles show the temperature dependence of the scale factors for the  $R$ -based and  $\tau_{353}$ -based  $N_H$  maps, respectively, and the gray bands show the systematic uncertainty (see the text in Section 4.1.2 for details). Points for the  $R$ -based analysis were shifted horizontally to the right by 0.05 K for display. Although a small fraction of the pixels have  $T_d$  below 18 K or above 22 K, they are included in the first and last data points, respectively.

distribution and the halo height typically most strongly affect the propagated CR spatial distribution (in the Galactocentric distance and the height from the Galactic plane), and therefore the IC spatial distribution (in  $l$  and  $b$ ). Therefore, we tested two additional CR source distributions, the pulsar-based distribution by Lorimer et al. (2006) and the supernova remnant (SNR)-based distribution by Case & Bhattacharya (1998), and one additional CR halo height, 10 kpc; these are also available in Ackermann et al. (2012a), where the diffusion coefficient was adjusted when changing the CR source distribution and halo height to match the direct CR measurements at the Earth’s surface. The obtained IC maps show the smallest gradient in the Galactic longitude direction with the SNR-based CR source distribution (the flattest distribution of our three choices) and the smallest gradient in the Galactic latitude direction with  $z_h = 10$  kpc (the larger halo height of our two choices). These tests result in a very small variation in the scaling factors (comparable to the statistical errors) in the case of the  $R$ -based  $N_H$  template maps. This is due to the small normalization of the IC terms, which is nearly 0, as exemplified by Table 1, and likely underestimates the systematic uncertainty. Therefore, we also employed a fit using our baseline IC model in which the normalization of the IC term was fixed to 1.0. While the scale factors were found to be robust against fixing the IC normalization to 1.0 for the case of the  $\tau_{353}$ -based analysis, the scale factors for the  $R$ -based analysis decreased by  $\sim 10\%$ . The systematic uncertainty due to the choice of IC model, evaluated as described above, is shown by the shaded bands in Figure 7. We found that the  $T_d$  dependence seen for the  $\tau_{353}$ -based analysis is robust against systematic uncertainties examined here, while that for the  $R$ -based analysis is less significant (scale factors of each  $T_d$  range are roughly the same within errors) if not zero. We also tested the alternative Sun/Moon emission model (see Section 4.1.1) and confirmed that the change in the  $T_d$  dependence of the scale factors for the  $R$ -based analysis is  $\leq 1\%$  and negligible compared to the systematic uncertainty due to the IC modeling.

In Figure 7, we observed a clear positive  $T_d$  dependence for  $N_H/\tau_{353}$ . This trend implies an underestimation of the  $N_H/\tau_{353}$  ratio in low-temperature areas and cannot be interpreted as being due to the properties of CRs, because the physical parameters that determine  $\tau_{353}$  (e.g., dust-to-gas ratio or the dust cross section at 353 GHz) do not affect the CR intensity. The only possible explanation in terms of the CR properties is the exclusion of charged particles in dense clouds with large magnetic fields expected in areas of low  $T_d$ . However, CRs have been confirmed to penetrate into dense cloud cores with  $W_{\text{CO}} \geq 10 \text{ K km s}^{-1}$  (e.g., [Abdo et al. 2010](#); [Ackermann et al. 2011, 2012b](#)), which corresponds to densities much larger than those of the clouds studied here with conventional values of  $X_{\text{CO}}$ . With  $X_{\text{CO}} = (1-2) \times 10^{20} \text{ cm}^{-2} \text{ K}^{-1} (\text{km s}^{-1})^{-1}$  inferred in nearby clouds (e.g., [Grenier et al. 2015](#)), we would have  $N_H = (2-4) \times 10^{21} \text{ cm}^2$  for  $W_{\text{CO}} = 10 \text{ K km s}^{-1}$ ; this is larger than for the densest clouds in the region studied (see Figures 1 and 2). Indeed,  $c_{1,i}(E)$  in Table 2 shows that the trend in Figure 7 is seen in both the low- and high-energy bands. Therefore, the main cause of the  $T_d$  dependence found here is not the properties of the CRs. Instead, it suggests that the dust opacity increases as  $T_d$  decreases.

**Table 1.** Results with the  $R$ -based  $N_H$  maps sorted by  $T_d$  in the northern region

Energy (GeV)	$c_{1,1}$ ( $T_d \leq 19 \text{ K}$ )	$c_{1,2}$ (19–20 K)	$c_{1,3}$ (20–21 K)	$c_{1,4}$ ( $T_d \geq 21 \text{ K}$ )	$c_2$	$c_3$	$I_{\text{iso}}$ (intensity <sup>a</sup> )	$I_{\text{iso}}$ (index)
0.2–0.4	$0.89 \pm 0.04$	$0.77 \pm 0.04$	$0.96 \pm 0.03$	$0.78 \pm 0.06$	$\leq 0.20$	$1.14 \pm 0.06$	$40.7 \pm 0.4$	$2.28 \pm 0.01$
0.4–0.8	$0.99 \pm 0.04$	$0.89 \pm 0.03$	$0.99 \pm 0.02$	$0.87 \pm 0.05$	$\leq 0.10$	$1.31 \pm 0.10$	$16.1 \pm 0.2$	$2.27 \pm 0.02$
0.8–1.6	$1.00 \pm 0.05$	$0.96 \pm 0.05$	$1.05 \pm 0.04$	$0.92 \pm 0.07$	$\leq 0.31$	$1.38 \pm 0.12$	$6.02 \pm 0.17$	$2.44 \pm 0.02$
1.6–3.2	$1.02 \pm 0.06$	$0.97 \pm 0.05$	$1.05 \pm 0.04$	$0.91 \pm 0.07$	$\leq 0.17$	$1.20 \pm 0.17$	$2.23 \pm 0.06$	$2.31 \pm 0.04$
3.2–6.4	$0.99 \pm 0.10$	$0.89 \pm 0.08$	$1.03 \pm 0.07$	$0.86 \pm 0.13$	$\leq 0.38$	$1.12 \pm 0.26$	$0.99 \pm 0.04$	$2.25 \pm 0.06$
6.4–12.8	$1.44 \pm 0.21$	$1.17 \pm 0.18$	$1.23 \pm 0.16$	$1.04 \pm 0.27$	$\leq 1.16$	$1.73 \pm 0.43$	$0.34 \pm 0.04$	$2.44 \pm 0.10$

<sup>a</sup>The integrated intensity ( $10^{-7} \text{ ph s}^{-1} \text{ cm}^{-2} \text{ sr}^{-1}$ ) in each band.

NOTE— The errors are the 1-sigma statistical uncertainties. Each of the four scale factors ( $c_{1,1}$ ,  $c_{1,2}$ ,  $c_{1,3}$ , and  $c_{1,4}$ ) gives the normalization for a specified range of  $T_d$  of the neutral-gas template in each energy bin.  $c_2$  and  $c_3$  give the normalizations for the IC and the  $\gamma$ -ray emission from the Sun and Moon, respectively, in each energy bin.  $I_{\text{iso}}$  is modeled using a power law with the integrated intensity and the photon index as free parameters.

**Table 2.** Results with the  $\tau_{353}$ -based  $N_{\text{H}}$  maps sorted by  $T_{\text{d}}$  in the northern region

Energy (GeV)	$c_{1,1}$ ( $T_{\text{d}} \leq 19$ K)	$c_{1,2}$ (19–20 K)	$c_{1,3}$ (20–21 K)	$c_{1,4}$ ( $T_{\text{d}} \geq 21$ K)	$c_2$	$c_3$	$I_{\text{iso}}$ (intensity <sup>a</sup> )	$I_{\text{iso}}$ (index)
0.2–0.4	$0.54 \pm 0.03$	$0.49 \pm 0.03$	$0.70 \pm 0.02$	$0.76 \pm 0.06$	$0.39 \pm 0.14$	$0.88 \pm 0.07$	$41.0 \pm 0.7$	$2.25 \pm 0.01$
0.4–0.8	$0.60 \pm 0.02$	$0.58 \pm 0.02$	$0.77 \pm 0.02$	$0.83 \pm 0.05$	$\leq 0.24$	$0.86 \pm 0.10$	$17.4 \pm 0.3$	$2.26 \pm 0.01$
0.8–1.6	$0.61 \pm 0.03$	$0.65 \pm 0.02$	$0.82 \pm 0.02$	$0.91 \pm 0.06$	$0.29 \pm 0.24$	$1.00 \pm 0.13$	$6.25 \pm 0.22$	$2.43 \pm 0.02$
1.6–3.2	$0.60 \pm 0.04$	$0.63 \pm 0.03$	$0.80 \pm 0.03$	$0.85 \pm 0.08$	$\leq 0.34$	$0.87 \pm 0.17$	$2.46 \pm 0.07$	$2.33 \pm 0.03$
3.2–6.4	$0.61 \pm 0.06$	$0.62 \pm 0.06$	$0.83 \pm 0.06$	$0.85 \pm 0.14$	$\leq 0.48$	$0.89 \pm 0.25$	$1.04 \pm 0.04$	$2.27 \pm 0.05$
6.4–12.8	$0.91 \pm 0.14$	$0.80 \pm 0.12$	$0.96 \pm 0.13$	$1.01 \pm 0.28$	$\leq 1.34$	$1.53 \pm 0.43$	$0.35 \pm 0.04$	$2.46 \pm 0.10$

<sup>a</sup>The integrated intensity ( $10^{-7}$  ph s<sup>-1</sup> cm<sup>-2</sup> sr<sup>-1</sup>) in each band.

NOTE— The errors are the 1-sigma statistical uncertainties. Each of the four scale factors ( $c_{1,1}$ ,  $c_{1,2}$ ,  $c_{1,3}$ , and  $c_{1,4}$ ) gives the normalization for a specified range of  $T_{\text{d}}$  of the neutral-gas template in each energy bin.  $c_2$  and  $c_3$  give the normalizations for the IC and the  $\gamma$ -ray emission from the Sun and Moon, respectively, in each energy bin.  $I_{\text{iso}}$  is modeled using a power law with the integrated intensity and the photon index as free parameters.

4.1.3. *Final Modeling*

As shown in Section 4.1.2, while the  $\gamma$ -ray data analysis reveals that the  $N_{\text{H}}/\tau_{353}$  ratio has a positive  $T_{\text{d}}$  dependence, the  $N_{\text{H}}/R$  ratio is rather constant. Because an  $R$ -based analysis was still preferred in terms of  $\ln L$  in  $T_{\text{d}}$ -sorted modeling, we used  $R$  to construct our best estimate of the  $N_{\text{H}}$  distribution. Within the systematic uncertainties, no dependence on  $T_{\text{d}}$  is indicated (see Figure 7); therefore, applying a simple correction such as a linear function of  $T_{\text{d}}$  to the conversion factor for  $R$  ( $38.4 \times 10^{26} \text{ cm}^{-2} (\text{W m}^{-2} \text{ sr}^{-1})^{-1}$ ) is not necessary. The most noticeable feature in Figure 7 is an apparent decrease in the scaling factor for  $T_{\text{d}} \geq 21 \text{ K}$  where the conversion from  $R$  to  $N_{\text{H}}$  was calibrated (Section 4.1). To examine whether this marked decrease is robust, we performed a further analysis using two  $T_{\text{d}}$ -sorted  $N_{\text{H}}$  maps, one with  $T_{\text{d}} \leq 21 \text{ K}$ , and the other with  $T_{\text{d}} \geq 21 \text{ K}$ . The obtained scale factors for the neutral-gas template agree within 1% for the low and high  $T_{\text{d}}$  maps when averaged over the entire energy band. We also tested other thresholds of  $T_{\text{d}}$  (19.0 K and 20.0 K) and confirmed that the scaling factors agree within 1% for the low and high  $T_{\text{d}}$  maps. These results indicate that there is no strong statistical evidence for a  $T_{\text{d}}$  dependence and therefore the single  $R$ -based  $N_{\text{H}}$  map is preferred. Therefore we adopt it as our best estimate of the  $N_{\text{H}}$  distribution. Finally, we fit the  $\gamma$ -ray data using this map (in the same way as in Section 4.1.1) but with finer energy bins, in order to study the spectral shape in more detail; each band was divided into two sub-bands. We summarize the best-fit model parameters and the obtained spectral components in Table 3 and Figure 8, respectively.

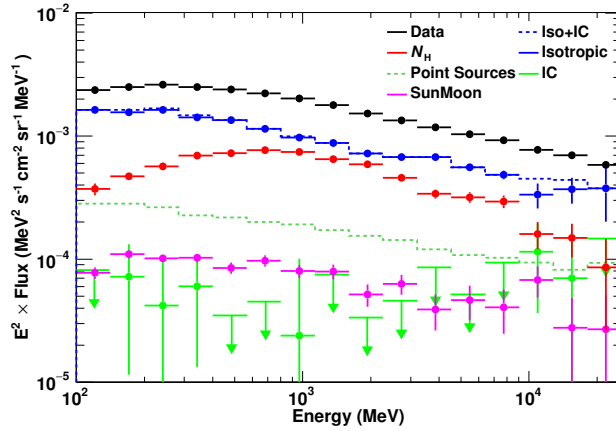


**Figure 8.** The spectrum of each component obtained from the fit with the single,  $R$ -based  $N_{\text{H}}$  map in the northern region. The sum of the isotropic and IC components is also shown for reference. The expected flux of the  $N_{\text{HII}}$  model is  $\sim 100$  times smaller than the flux of  $N_{\text{H}}$  model and is below the vertical axis range.

**Table 3.** Results of the fit with the  $R$ -based single  $N_{\text{H}}$  map in the northern region

Energy (GeV)	$c_1$	$(E^2 \cdot c_1 \cdot q_\gamma)^{\text{a}}$	$c_2$	$c_3$	$I_{\text{iso}}$ (norm <sup>b</sup> )	$I_{\text{iso}}$ (index)
0.10–0.14	$0.93 \pm 0.10$	1.11	$\leq 0.29$	$0.88 \pm 0.09$	$48.1 \pm 1.4$	$1.93 \pm 0.05$
0.14–0.20	$0.87 \pm 0.06$	1.41	$0.27 \pm 0.23$	$1.17 \pm 0.09$	$32.7 \pm 1.0$	$2.06 \pm 0.05$
0.20–0.28	$0.84 \pm 0.04$	1.71	$0.18 \pm 0.24$	$1.15 \pm 0.08$	$24.1 \pm 0.5$	$2.26 \pm 0.03$
0.28–0.40	$0.91 \pm 0.03$	2.12	$0.28 \pm 0.22$	$1.26 \pm 0.10$	$14.8 \pm 0.4$	$2.30 \pm 0.04$
0.40–0.57	$0.93 \pm 0.03$	2.22	$\leq 0.18$	$1.15 \pm 0.12$	$9.93 \pm 0.17$	$2.25 \pm 0.04$
0.57–0.80	$1.00 \pm 0.03$	2.37	$\leq 0.26$	$1.47 \pm 0.15$	$5.97 \pm 0.14$	$2.28 \pm 0.05$
0.80–1.13	$1.04 \pm 0.05$	2.30	$0.18 \pm 0.49$	$1.34 \pm 0.18$	$3.56 \pm 0.21$	$2.28 \pm 0.06$
1.13–1.60	$0.99 \pm 0.05$	2.00	$\leq 0.52$	$1.45 \pm 0.20$	$2.29 \pm 0.17$	$2.52 \pm 0.08$
1.60–2.26	$1.05 \pm 0.04$	1.84	$\leq 0.26$	$1.06 \pm 0.22$	$1.33 \pm 0.05$	$2.30 \pm 0.10$
2.26–3.20	$0.98 \pm 0.05$	1.42	$\leq 0.39$	$1.43 \pm 0.26$	$0.87 \pm 0.04$	$2.23 \pm 0.11$
3.20–4.53	$0.91 \pm 0.08$	1.05	$\leq 0.80$	$0.99 \pm 0.32$	$0.62 \pm 0.04$	$2.48 \pm 0.13$
4.53–6.40	$1.12 \pm 0.11$	0.99	$\leq 0.54$	$1.34 \pm 0.42$	$0.36 \pm 0.02$	$2.20 \pm 0.18$
6.40–9.05	$1.36 \pm 0.16$	0.92	$\leq 1.10$	$1.34 \pm 0.53$	$0.22 \pm 0.02$	$2.52 \pm 0.23$
9.05–12.8	$0.97 \pm 0.24$	0.50	$1.54 \pm 1.05$	$2.57 \pm 0.73$	$0.11 \pm 0.03$	$1.87 \pm 0.38$
12.8–18.1	$1.17 \pm 0.36$	0.46	$1.08 \pm 1.38$	$1.22 \pm 0.91$	$0.08 \pm 0.02$	$2.01 \pm 0.39$
18.1–25.6	$0.87 \pm 0.60$	0.27	$\leq 2.64$	$1.40 \pm 1.24$	$0.06 \pm 0.03$	$2.36 \pm 0.39$

<sup>a</sup>The emissivity ( $c_1 \times q_\gamma$ ) multiplied by  $E^2$  where  $E = \sqrt{E_{\text{min}}E_{\text{max}}}$  in each energy bin in units of  $10^{-24} \text{ MeV}^2 \text{ s}^{-1} \text{ cm}^{-2} \text{ sr}^{-1} \text{ MeV}^{-1}$ .

<sup>b</sup>The integrated intensity ( $10^{-7} \text{ ph s}^{-1} \text{ cm}^{-2} \text{ sr}^{-1}$ ) in each band.

NOTE— The errors are the 1-sigma statistical uncertainties.  $c_1$ ,  $c_2$ , and  $c_3$  give the normalizations for the neutral-gas template, IC, and the  $\gamma$ -ray emission from the Sun and Moon, respectively, in each energy bin.  $I_{\text{iso}}$  is modeled using a power law with the integrated intensity and the photon index as free parameters. For convenience, the best-fit value of the emissivity multiplied by  $E^2$  is also tabulated.



## 4.2. Southern Region

### 4.2.1. Initial Modeling with a Single Gas Map

We then proceeded to model the southern region in which the same analysis procedures were used as for the northern region. Since the ecliptic plane does not run through the ROI, we fixed the scale factors for the Sun and Moon emission template to 1.0. The  $N_{\text{H}}$  model maps were prepared as described in Section 2.2: We used  $N_{\text{H}}(\text{cm}^{-2}) = 1.82 \times 10^{18} \cdot W_{\text{HI}}(\text{K km s}^{-1})$ , or  $N_{\text{H}}(\text{cm}^{-2}) = 32.0 \times 10^{26} \cdot R(\text{W m}^{-2} \text{ sr}^{-1})$ , or  $N_{\text{H}}(\text{cm}^{-2}) = 122 \times 10^{24} \cdot \tau_{353}$ . As a side effect of masking the Orion-Eridanus superbubble, the  $N_{\text{H}}$  template map has a similar spatial distribution (larger intensity toward the Galactic center) to that of the IC model and they are degenerate with each other. As we progressed in the iterative method, we observed that the  $N_{\text{H}}$  template is given progressively lower scale factor ( $c_1$ ) while the IC component is given higher one ( $c_2$ ) in low-energy bands, although the contribution of point sources to the total  $\gamma$ -ray flux is almost unchanged. To mitigate this, we employed a (semi-)global fitting as a preparatory stage. We first adopted wider energy bins allowing overlaps (70.7–282.8 MeV, 141.4–565.7 MeV, etc.), and we included point sources iteratively until the fit improvement is saturated as we did for the analysis of the northern region. Allowing overlapping the energy bins makes the fit results more stable by encouraging spectral inter-bin consistency. We then fixed the IC normalization to the best-fit value and repeated the analysis with the original energy bins (100–200 MeV, 200–400 MeV, etc.). This “two-stage” analysis is employed hereafter for the southern region.

The obtained log-likelihoods, summed over individual energy ranges in 0.1–25.6 GeV with the  $R$ -based and  $\tau_{353}$ -based  $N_{\text{H}}$  maps are 19.4 and  $-74.6$ , respectively, when compared to that of the  $W_{\text{HI}}$ -based  $N_{\text{H}}$  map. Therefore, the  $R$ -based  $N_{\text{H}}$  map is preferred compared to the  $\tau_{353}$ -based map. Like the northern region, this conclusion is unchanged against the significance threshold of point source model or the lowest energy threshold. The averages of the normalization for the neutral gas component,  $c_1$  in Equation (1), are  $0.946 \pm 0.008$ ,  $0.946 \pm 0.007$ , and  $0.690 \pm 0.005$  for the  $W_{\text{HI}}$ -based,  $R$ -based, and  $\tau_{353}$ -based maps, respectively. The residual maps are summarized in Figure 9.

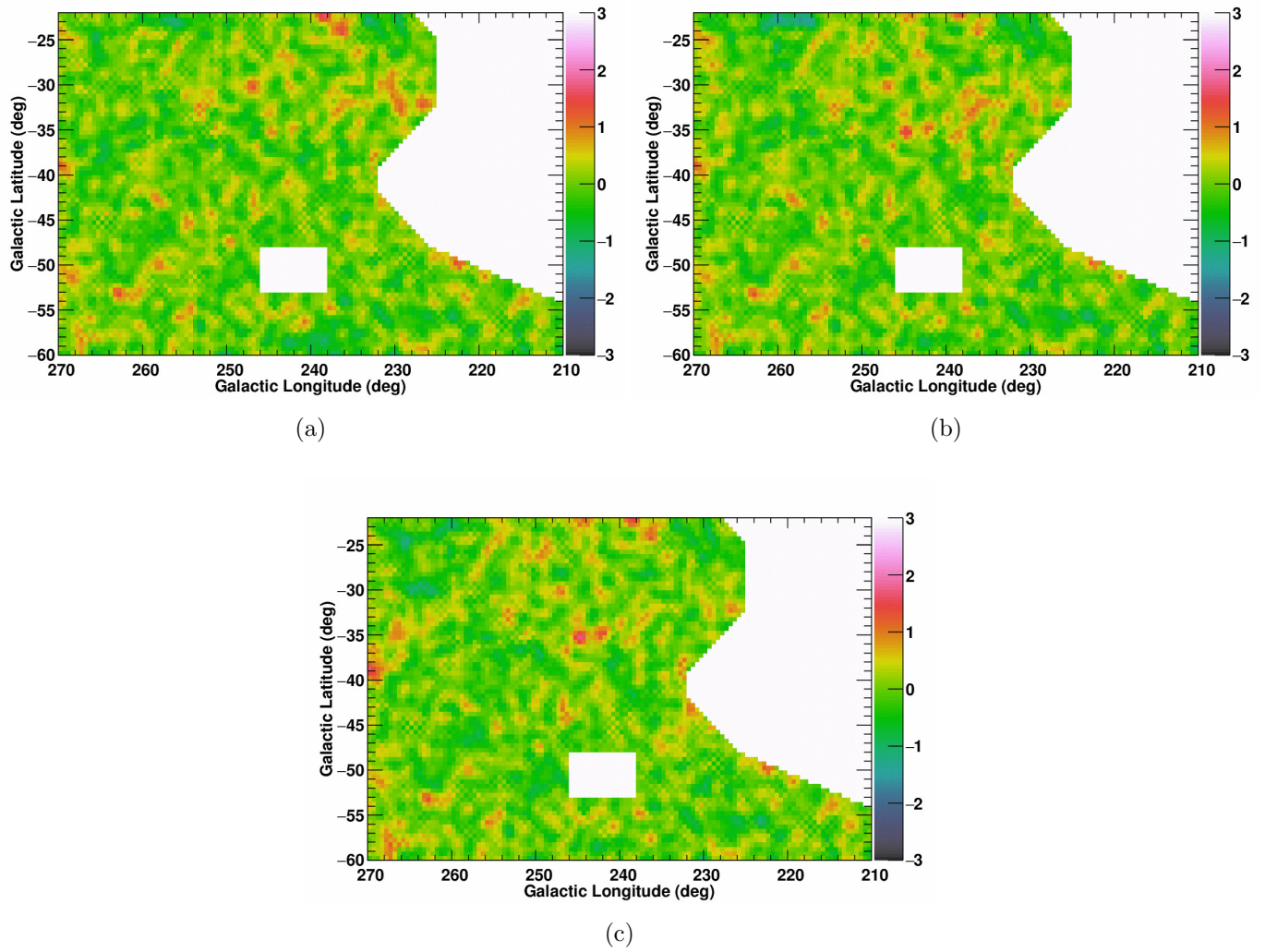


**Figure 9.** The same as Figure 6 but for the southern region instead of the northern region.

4.2.2. *Dust Emission-Sorted Modeling*

As we saw in Section 2.1 (Figure 2), the correlation between  $W_{\text{HI}}$  and  $D_{\text{em}}$  shows a change of the slope in particular for  $\tau_{353}$  while the  $T_{\text{d}}$  dependence is small; unlike the case of the northern region, the  $W_{\text{HI}}-D_{\text{em}}$  relationship depends on  $D_{\text{em}}$  rather than  $T_{\text{d}}$ . Even though the  $R$ -based  $N_{\text{H}}$  map is preferred for the three models in terms of  $\ln L$ , the true  $N_{\text{H}}$  distribution could be appreciably different and a possible nonlinear relationship between  $N_{\text{H}}$  and  $D_{\text{em}}$  should be examined. Therefore, we performed an analysis with  $R$ -sorted and  $\tau_{353}$ -sorted  $N_{\text{H}}$  maps (instead of  $T_{\text{d}}$ -sorted  $N_{\text{H}}$  maps applied for the northern region). We split the  $N_{\text{H}}$  template map (constructed from  $R$ ) into three templates based on  $R$ , for  $R \leq 12$ ,  $R = 12-20$ , and  $R \geq 20$  in units of  $10^{-8} \text{ W m}^{-2} \text{ sr}^{-1}$ <sup>17</sup>, and fit the  $\gamma$ -ray data with Equation (1), using  $\sum_i c_{1,i}(E) \cdot N_{\text{H},i}(l, b)$  instead of  $c_1(E) \cdot N_{\text{H}}(l, b)$ , where  $c_{1,i}(E)$  and  $N_{\text{H},i}(l, b)$  represent the scale factor and template gas map for each of the three templates. For the  $\tau_{353}$ -based  $N_{\text{H}}$  template, we split it into three as  $\tau_{353} \leq 4$ ,  $\tau_{353} = 4-6$ , and  $\tau_{353} \geq 6$  in units of  $10^{-6}$ <sup>18</sup>. With a plausible assumption of a uniform CR intensity,  $c_{1,i}(E)$  is expected to trace the  $N_{\text{H}}/D_{\text{em}}$  ratio. We used data in the range of 0.2–12.8 GeV to avoid a possible unstable fit in the lowest (0.1–0.2 GeV) and highest (12.8–25.6 GeV) energy bands; then, we obtained a value of TS of 22.0 and 101.8 for  $R$  and  $\tau_{353}$ , respectively, with 18 more degrees of freedom. This indicates a  $7.4\sigma$  improvement when the  $\tau_{353}$  model for  $N_{\text{H}}$  is used, while the improvement of the fit is not significant for  $R$ . We also note that  $\tau_{353}$ -sorted modeling is still not favored compared to the analysis using the single  $N_{\text{H}}$  map based on  $R$  in terms of  $\ln L$ . The  $R$ - and  $\tau_{353}$ -dependence of the scaling factors is summarized in Tables 4 and 5, and the averages over 0.2–12.8 GeV are summarized in Figure 10.

As for the northern region, we examined the systematic uncertainty due to the choice of the IC model and plotted the results in Figure 10; the outer polygonal area shows the full uncertainty evaluated by trying all six IC models, and the inner, shaded area shows the variation where the model with the worst  $\ln L$  was excluded. One may also argue that the obtained scale factors of the IC term and the isotropic emission intensity are greatly different between the northern and southern ROIs (Tables 1, 2, 4, and 5), and that the IC normalization is nearly 0 (which is not physical) with the  $R$ -based  $N_{\text{H}}$  template fit for the northern region. This indicates that our model does not completely describe the  $\gamma$ -ray data. For example, the IC spatial template may not agree with the true distribution, or there may be a small variation of the (quasi-) isotropic component. If the IC spatial template is not representing the underlying distribution of the IC emission observed by the LAT, it will most likely be ingested in the isotropic component contributions. Therefore it is the total IC and isotropic that matters for these particular ROIs, and the sum of the IC term and isotropic emission is similar between two ROIs (Figures 8 and 11). Therefore, most of uncertainties of the IC term and the isotropic emission are mutually absorbed, and we believe that the effect on the neutral gas component is properly examined by employing several IC models as described above and in Section 4.1.2. We also note that while the differences of log-likelihoods are very small (19.4) between the  $R$ -based model and the  $W_{\text{HI}}$ -based one, the specific choice of the template does not affect the gas (and CR) properties very much; the normalizations of the neutral gas component are almost identical between the two gas models as described in Section 4.2.1.

<sup>17</sup> For information, the relative values of the integral of  $R \times$  solid angle (proportional to the relative flux with uniform CR intensity) are 65.8%, 25.5%, and 8.7% for  $R \leq 12$ ,  $R = 12-20$ , and  $R \geq 20$  in units of  $10^{-8} \text{ W m}^{-2} \text{ sr}^{-1}$ , respectively.

<sup>18</sup> For information, the relative values of the integral of  $\tau_{353} \times$  solid angle (proportional to the relative flux with uniform CR intensity) are 67.1%, 17.4%, and 15.5% for  $\tau_{353} \leq 4$ ,  $\tau_{353} = 4-6$ , and  $\tau_{353} \geq 6$  in units of  $10^{-6}$ , respectively.

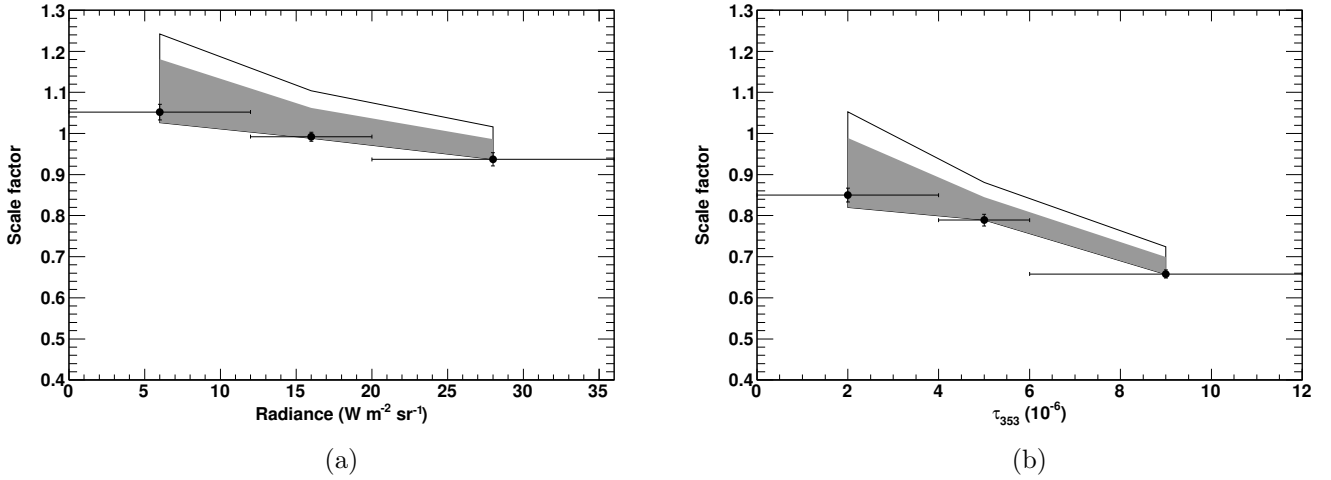


**Figure 10.** Summary of the scale factor  $c_{1,i}$  in Equation (1) averaged over 0.2–12.8 GeV in each range of  $R$  (a) and  $\tau_{353}$  (b). The outer polygonal area shows the systematic uncertainty evaluated using all six IC models, and the inner, shaded area shows the uncertainty where the model with the worst  $\ln L$  was excluded. Although a small fraction of the pixels show  $D_{\text{em}}$  above the horizontal axis ranges, they are included in the last data points.

In Figure 10, we observe a clear negative  $\tau_{353}$  dependence of the scale factor that is robust against the systematics due to the choice of IC model. This trend implies an overestimation of the  $N_{\text{H}}/\tau_{353}$  ratio in the high-density area. As discussed in Section 4.1.2, this cannot be interpreted as being due to the properties of CRs. Instead, it is likely due to the dust properties, such as the change of the dust cross section by dust grain evolution (e.g., Roy et al. 2013). For the case of  $R$ -sorted analysis, there seems to be a negative dependence. However, the change of  $N_{\text{H}}/R$  ratio (inversely proportional to the scale factor) is much smaller than that for  $\tau_{353}$  whatever IC model is employed, and the fit improvement is not significant. Therefore an  $R$ -based single  $N_{\text{H}}$  map is suggested to reproduce the  $N_{\text{H}}$  distribution inferred by  $\gamma$ -ray data.

**Table 4.** Results with the  $R$ -based  $N_{\text{H}}$  maps sorted by  $R$  in the southern region

Energy (GeV)	$c_{1,1}$ ( $R^{\text{a}} \leq 12$ )	$c_{1,2}$ (12–20)	$c_{1,3}$ ( $R \geq 20$ )	$c_2$	$I_{\text{iso}}$ (norm <sup>b</sup> )	$I_{\text{iso}}$ (index)
0.2–0.4	$1.00 \pm 0.04$	$0.88 \pm 0.02$	$0.88 \pm 0.03$	$2.72 \pm 0.10$	$23.6 \pm 0.3$	$2.35 \pm 0.02$
0.4–0.8	$1.04 \pm 0.03$	$1.01 \pm 0.02$	$0.91 \pm 0.03$	$2.32 \pm 0.14$	$9.97 \pm 0.16$	$2.33 \pm 0.03$
0.8–1.6	$1.11 \pm 0.04$	$1.09 \pm 0.02$	$1.02 \pm 0.04$	$2.53 \pm 0.19$	$3.41 \pm 0.08$	$2.46 \pm 0.05$
1.6–3.2	$1.07 \pm 0.06$	$1.01 \pm 0.04$	$1.02 \pm 0.05$	$2.56 \pm 0.26$	$1.18 \pm 0.05$	$2.25 \pm 0.08$
3.2–6.4	$1.01 \pm 0.11$	$1.09 \pm 0.07$	$0.87 \pm 0.09$	$2.37 \pm 0.38$	$0.57 \pm 0.03$	$2.14 \pm 0.11$
6.4–12.8	$1.36 \pm 0.22$	$1.15 \pm 0.13$	$0.96 \pm 0.17$	$3.07 \pm 0.58$	$0.19 \pm 0.02$	$2.83 \pm 0.20$

<sup>a</sup> $R$  is given in units of  $10^{-8} \text{ W m}^{-1} \text{ sr}^{-1}$

<sup>b</sup>The integrated intensity ( $10^{-7} \text{ ph s}^{-1} \text{ cm}^{-2} \text{ sr}^{-1}$ ) in each band.

NOTE— The errors are the 1-sigma statistical uncertainties. Each of the three scale factors ( $c_{1,1}$ ,  $c_{1,2}$ , and  $c_{1,3}$ ) gives the normalization for a specified range of  $R$  of the neutral-gas template in each energy bin.  $c_2$  is the IC template normalization for each energy bin obtained at the first stage of the fitting (see text).  $I_{\text{iso}}$  is modeled using a power law with the integrated intensity and the photon index as free parameters.

**Table 5.** Results with the  $\tau_{353}$ -based  $N_{\text{H}}$  maps sorted by  $\tau_{353}$  in the southern region

Energy (GeV)	$c_{1,1}$ ( $\tau_{353}^{\text{a}} \leq 4$ )	$c_{1,2}$ (4–6)	$c_{1,3}$ ( $\tau_{353} \geq 6$ )	$c_2$	$I_{\text{iso}}$ (norm <sup>b</sup> )	$I_{\text{iso}}$ (index)
0.2–0.4	$0.84 \pm 0.04$	$0.67 \pm 0.03$	$0.64 \pm 0.02$	$3.01 \pm 0.10$	$22.7 \pm 0.3$	$2.33 \pm 0.02$
0.4–0.8	$0.83 \pm 0.03$	$0.82 \pm 0.03$	$0.63 \pm 0.02$	$2.85 \pm 0.13$	$9.35 \pm 0.15$	$2.31 \pm 0.03$
0.8–1.6	$0.87 \pm 0.03$	$0.85 \pm 0.03$	$0.71 \pm 0.02$	$3.15 \pm 0.18$	$3.15 \pm 0.08$	$2.47 \pm 0.05$
1.6–3.2	$0.89 \pm 0.05$	$0.78 \pm 0.04$	$0.70 \pm 0.03$	$3.06 \pm 0.25$	$1.07 \pm 0.04$	$2.27 \pm 0.09$
3.2–6.4	$0.80 \pm 0.09$	$0.91 \pm 0.07$	$0.60 \pm 0.05$	$2.83 \pm 0.37$	$0.54 \pm 0.03$	$2.16 \pm 0.12$
6.4–12.8	$1.00 \pm 0.18$	$0.87 \pm 0.15$	$0.63 \pm 0.10$	$3.54 \pm 0.54$	$0.18 \pm 0.02$	$2.33 \pm 0.21$

<sup>a</sup> $\tau_{353}$  is given in units of  $10^{-6}$

<sup>b</sup>The integrated intensity ( $10^{-7} \text{ ph s}^{-1} \text{ cm}^{-2} \text{ sr}^{-1}$ ) in each band.

NOTE— The errors are the 1-sigma statistical uncertainties. Each of the three scale factors ( $c_{1,1}$ ,  $c_{1,2}$ , and  $c_{1,3}$ ) gives the normalization for a specified range of  $\tau_{353}$  of the neutral-gas template in each energy bin.  $c_2$  is the IC template normalization for each energy bin obtained at the first stage of the fitting (see text).  $I_{\text{iso}}$  is modeled using a power law with the integrated intensity and the photon index as free parameters.

4.2.3. *Final Modeling*

We employed the  $\gamma$ -ray data as a robust tracer of the total neutral gas distribution. We therefore can apply a correction to the  $N_{\text{H}}$  model template based on  $\gamma$ -ray data in principle. To prove this concept, and to see if this affects the choice of dust tracer ( $R$  or  $\tau_{353}$ ), we started with the uncorrected  $N_{\text{H}}$  map that is proportional to  $\tau_{353}$  (denoted as  $N_{\text{H},\tau_{353}}$ ) and modified the gas column density to take into account the observed  $\tau_{353}$ -dependence (Figure 10). We assumed that the  $N_{\text{H}}$  is proportional to  $\tau_{353}$  up to a particular value ( $\tau_{\text{bk}}$ ) and deviates from the proportionality linearly above that. Then, we can apply the correction to the  $N_{\text{H}}$  model using the empirical function below:

$$N_{\text{H,mod}} = \begin{cases} N_{\text{H},\tau_{353}} & (\tau_{353} < \tau_{\text{bk}}) , \\ N_{\text{H,bk}} + (1 - 0.1 \cdot C) \cdot (N_{\text{H},\tau_{353}} - N_{\text{H,bk}}) & (\tau_{353} \geq \tau_{\text{bk}}) , \end{cases} \quad (2)$$

where  $N_{\text{H,bk}}$  is the (uncorrected) gas column density (proportional to  $\tau_{353}$ ) at  $\tau_{\text{bk}}$ .  $C = 1$  corresponds to a 10% decrease in  $N_{\text{H}}$  above  $N_{\text{H,bk}}$ . We carried out a grid scan ( $\tau_{\text{bk}}=2, 3, 4, 5, 6$  in unit of  $10^{-6}$  and  $C=2, 3, 4, 5, 6$ ) and found that  $\tau_{\text{bk}} = 4$  and  $C = 4$  gives the best representation of the *Fermi*-LAT data. This configuration increases the scale factor of the neutral gas component by 20% and makes it agree with that from the  $R$ -based one within 15%.

The corrected  $N_{\text{H}}$  model based on  $\tau_{353}$ , however, still gives smaller  $\ln L$  compared to the single  $N_{\text{H}}$  model based on  $R$ . Because we found that the  $R$ -dependence of the scaling factors of the neutral gas component is small if not zero, and the fit improvement is not significant over the single,  $R$ -based  $N_{\text{H}}$  template, we adopted this  $R$ -based  $N_{\text{H}}$  model as our best estimate of the  $N_{\text{H}}$  distribution. We, therefore, fit the  $\gamma$ -ray data using this map with finer energy bands to study the spectral shape in more detail as we did for the northern region. The best-fit model parameters and the obtained spectral components are summarized in Table 6 and Figure 11, respectively.

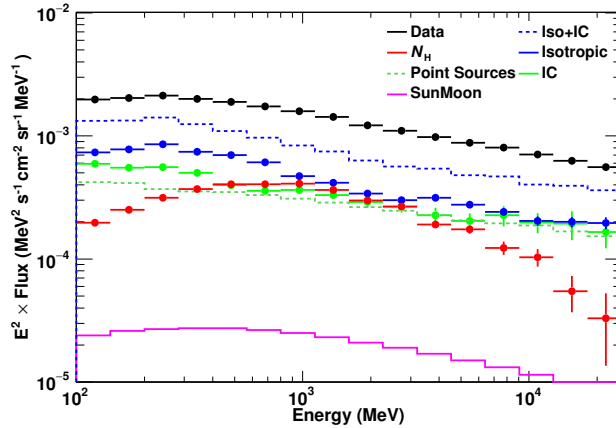


**Figure 11.** The spectrum of each component obtained from the fit based on the single,  $R$ -based  $N_{\text{H}}$  map in the southern region. The sum of the isotropic and IC components is also shown for reference. The expected flux of the  $N_{\text{H,II}}$  model is  $\sim 50$  times smaller than the flux of  $N_{\text{H}}$  model and is below the vertical axis range.



**Table 6.** Results of the fit with the  $R$ -based single  $N_{\text{H}}$  map in the southern region

Energy (GeV)	$c_1$	$(E^2 \cdot c_1 \cdot q_\gamma)^a$	$c_2$	$I_{\text{iso}}$ (norm <sup>b</sup> )	$I_{\text{iso}}$ (index)
0.10–0.14	$0.91 \pm 0.04$	1.08	$2.38 \pm 0.10$	$26.7 \pm 0.4$	$1.81 \pm 0.08$
0.14–0.20	$0.86 \pm 0.03$	1.40	$2.38 \pm 0.10$	$20.1 \pm 0.3$	$2.00 \pm 0.07$
0.20–0.28	$0.86 \pm 0.02$	1.76	$2.65 \pm 0.10$	$15.6 \pm 0.1$	$2.38 \pm 0.05$
0.28–0.40	$0.91 \pm 0.02$	2.11	$2.65 \pm 0.10$	$9.63 \pm 0.10$	$2.28 \pm 0.06$
0.40–0.57	$0.97 \pm 0.02$	2.34	$2.34 \pm 0.14$	$6.39 \pm 0.08$	$2.28 \pm 0.07$
0.57–0.80	$1.00 \pm 0.02$	2.36	$2.34 \pm 0.14$	$3.96 \pm 0.06$	$2.33 \pm 0.09$
0.80–1.13	$1.08 \pm 0.02$	2.39	$2.63 \pm 0.19$	$2.16 \pm 0.04$	$2.39 \pm 0.12$
0.13–1.60	$1.05 \pm 0.03$	2.13	$2.63 \pm 0.19$	$1.35 \pm 0.03$	$2.64 \pm 0.15$
1.60–2.26	$1.00 \pm 0.03$	1.76	$2.56 \pm 0.26$	$0.78 \pm 0.02$	$2.60 \pm 0.20$
2.26–3.20	$1.08 \pm 0.04$	1.57	$2.56 \pm 0.26$	$0.48 \pm 0.02$	$2.11 \pm 0.25$
3.20–4.53	$0.97 \pm 0.06$	1.12	$2.44 \pm 0.37$	$0.36 \pm 0.01$	$2.33 \pm 0.27$
4.53–6.40	$1.16 \pm 0.09$	1.03	$2.44 \pm 0.37$	$0.22 \pm 0.01$	$2.52 \pm 0.34$
6.40–9.05	$1.08 \pm 0.13$	0.72	$3.06 \pm 0.57$	$0.14 \pm 0.01$	$2.05 \pm 0.44$
9.05–12.8	$1.18 \pm 0.19$	0.61	$3.06 \pm 0.57$	$0.08 \pm 0.01$	$1.82 \pm 0.57$
12.8–18.1	$0.81 \pm 0.27$	0.32	$3.44 \pm 0.90$	$0.06 \pm 0.01$	$1.72 \pm 0.65$
18.1–25.6	$0.63 \pm 0.37$	0.19	$3.44 \pm 0.90$	$0.04 \pm 0.01$	$3.92 \pm 0.78$

<sup>a</sup>The emissivity ( $c_1 \times q_\gamma$ ) multiplied by  $E^2$  where  $E = \sqrt{E_{\text{min}}E_{\text{max}}}$  in each energy bin in units of  $10^{-24} \text{ MeV}^2 \text{ s}^{-1} \text{ cm}^{-2} \text{ sr}^{-1} \text{ MeV}^{-1}$ .

<sup>b</sup>The integrated intensity ( $10^{-7} \text{ ph s}^{-1} \text{ cm}^{-2} \text{ sr}^{-1}$ ) in each band.

NOTE— The errors are the 1-sigma statistical uncertainties.  $c_1$  and  $c_2$  give the normalization for the neutral-gas template and IC, respectively, in each energy bin (the best-fit values obtained at the first stage of the fitting are given for the latter).  $I_{\text{iso}}$  is modeled using a power law with the integrated intensity and the photon index as free parameters. For convenience, the best-fit value of the emissivity ( $c_1 \times q_\gamma$ ) multiplied by  $E^2$  is also tabulated.

## 5. DISCUSSION

## 5.1. ISM

In Section 4, we used the GeV  $\gamma$ -rays observed by *Fermi*-LAT as robust tracers of the ISM gas under the assumption of a uniform CR intensity and obtained the  $N_{\text{H}}$  distributions inferred by the  $\gamma$ -ray data. Trends of the scale factor for  $N_{\text{H}}$  templates ( $T_{\text{d}}$  dependence and  $\tau_{353}$  dependence in the northern and southern regions, respectively) are commonly seen between low- and high-energy bands (see Tables 1, 2, 4, and 5); this supports the uniformity of the CR intensity in each ROI. We found that the  $N_{\text{H}}$  template based on the  $R$  data best matches the  $\gamma$ -ray observations in both northern and southern regions and in the following discussion, we assume  $R$  is a good tracer of  $N_{\text{H}}$ . The obtained relationships between  $W_{\text{HI}}$  and  $N_{\text{H}}$  are shown in Figure 12 together with maps of the excess gas column density above  $N_{\text{HI}}^{\text{thin}}$ . We point out that the  $W_{\text{HI}}/\tau_{353}$  ratio (and  $N_{\text{H}}/\tau_{353}$  ratio) strongly depends on  $T_{\text{d}}$  in the northern region, while in the southern region this dependence is weaker. The dust optical depth  $\tau_{353}$  depends on  $T_{\text{d}}$  and the dust spectral index,  $\beta$ ; the two properties are tightly connected (Planck Collaboration XI 2014). The anti-correlation between  $T_{\text{d}}$  and  $\beta$  is apparent in the northern region while the southern region presents more dispersion. Differences in these dust properties suggest different grain evolution (e.g., Jones et al. 2013; Köhler et al. 2015). How this grain evolution is related to the observed  $\tau_{353}$  dependence of the  $N_{\text{H}}/\tau_{353}$  ratio in the southern region is not clear. In the following, we will focus on discussing implications of Figure 12.

In the northern region (panel (a)), the  $N_{\text{H}}/W_{\text{HI}}$  ratio in the area of low  $T_{\text{d}}$  (18–19 K) and high  $W_{\text{HI}}$  ( $\geq 300 \text{ K km s}^{-1}$ ) is greater than those in other areas. This area corresponds to the excess gas column density at around  $(l, b) = (236^\circ, 38^\circ.5)$  seen in panel (c). It also corresponds to the positive residual at around  $(l, b) = (236^\circ, 37^\circ.5)$  seen in the  $W_{\text{HI}}$ -based analysis (see also Figure 6(a) and Section 4.1.1). Because our ROI does not include strong CO emission (see Appendix C) and the data for the area of interest spans a wide range of  $W_{\text{HI}}$ , these gas-related emissions are likely due to optically thick HI and we will consider this scenario hereafter. The brightness temperature for the HI emission at the velocity  $v$  is given by

$$T_{\text{b}}(v) = [T_{\text{S}}(v) - T_{\text{bg}}] \cdot [1 - \exp(-\tau_{\text{HI}}(v))] \quad , \quad (3)$$

where  $T_{\text{bg}}$  is the background continuum radiation temperature, and  $T_{\text{S}}(v)$  and  $\tau_{\text{HI}}(v)$  are, respectively, a harmonic mean of the spin temperature at velocity  $v$  on the line of sight and an integration of the optical depth at this velocity. Then, if we approximate the HI emission spectrum by a single boxcar spectrum on the line of sight with a spectral width of  $\Delta V_{\text{HI}}$ ,  $T_{\text{S}}(v)$  and  $\tau_{\text{HI}}(v)$  can be expressed by single values independent of  $v$  and thus the  $W_{\text{HI}}$  can be correlated to  $N_{\text{H}}$  as a function of  $T_{\text{S}}$  such that (e.g., Fukui et al. (2015))

$$W_{\text{HI}}(\text{K km s}^{-1}) = [T_{\text{S}}(\text{K}) - T_{\text{bg}}(\text{K})] \cdot \Delta V_{\text{HI}}(\text{km s}^{-1}) \cdot [1 - \exp(-\tau_{\text{HI}})] \quad , \quad (4)$$

and

$$\tau_{\text{HI}} = \frac{N_{\text{Htot}}(\text{cm}^{-2})}{1.82 \times 10^{18}} \cdot \frac{1}{T_{\text{S}}(\text{K})} \cdot \frac{1}{\Delta V_{\text{HI}}(\text{km s}^{-1})} \quad , \quad (5)$$

where  $\Delta V_{\text{HI}}$  is defined as  $W_{\text{HI}}/(\text{peak HI brightness temperature})$ . In Figure 12(a), assuming that all of the gas is atomic, we overlaid the model curves for several choices of  $T_{\text{S}}$  with  $\Delta V_{\text{HI}} = 18 \text{ km s}^{-1}$  (the median linewidth in the northern region). As inferred from Figure 12(a), while most of the region is compatible with being optically thin, the area with  $T_{\text{d}} = 18\text{--}19 \text{ K}$  gives, on average,  $T_{\text{S}} \sim 40 \text{ K}$ .

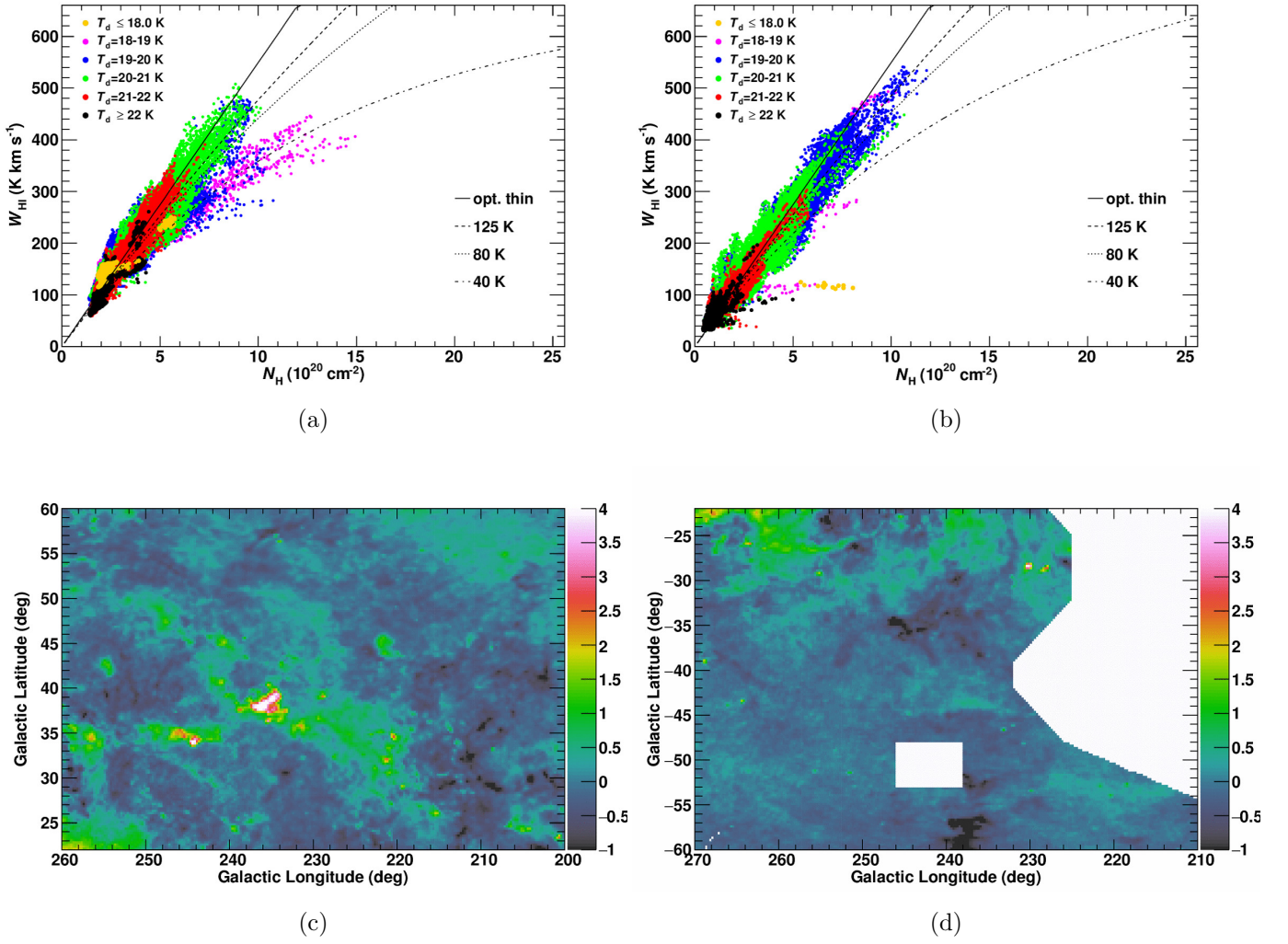


**Figure 12.** The correlation between  $W_{\text{HI}}$  and  $N_{\text{HI}}$  inferred from the  $\gamma$ -ray data analysis in the (a) northern and (b) southern regions, and the excess gas column density map (defined as  $N_{\text{HI}} - N_{\text{HI}}^{\text{thin}}$ ) in units of  $10^{20} \text{ cm}^{-2}$  in the (c) northern and (d) southern regions. The model curves for several choices of  $T_S$  are overlaid on panels (a) and (b).

In the southern region (Figure 12(b)), while most of the data lie along a mildly curved line, those in regions with  $T_d \leq 18 \text{ K}$  show a flat profile with  $W_{\text{HI}} \sim 100 \text{ K km s}^{-1}$  in the plot. This corresponds to a spot seen in the dust data at  $(l, b) \sim (230^\circ, -28^\circ.5)$  (see also Figure 12(d)); it is also seen in the residual map for the  $W_{\text{HI}}$ -based analysis (Figure 9(a)). A plausible interpretation is that the spot consists of CO-dark  $\text{H}_2$  (e.g., [Smith et al. 2014](#)) because the flat profile means that the column density of HI is nearly constant. Finally, we overlaid the model curves for several choices of  $T_S$  with  $\Delta V_{\text{HI}} = 21 \text{ km s}^{-1}$  (the median velocity of the southern region with several areas masked); the majority of data agree, on average, with the model curve for  $T_S = 125 \text{ K}$ , supporting the choice of  $T_S$  by [Abdo et al. \(2009b\)](#). This value also agrees well with the average value found in the local ISM,  $T_S = 140 \text{ K}$  ([Casandjian 2015](#)). We also note that there is a scatter around the model curve for  $T_S = 125 \text{ K}$ . Because  $W_{\text{HI}}$  and the optically-thin approximation gives the lower limit of  $N_{\text{HI}}$ , the

spread is likely because of the uncertainty of the  $D_{\text{em}}/N_{\text{H}}$  ratio, and thus could introduce over- and under-estimation of the  $N_{\text{H}}$ . For example, negative values of the excess gas column density are seen around  $(l, b) = (240^\circ, -35^\circ)$  in Figure 12(d), and they correspond to the residual (i.e., underestimate of  $N_{\text{H}}$ ) in Figure 9(b) and (c). This is a drawback of employing  $D_{\text{em}}$  as a tracer of the total gas column density, and the small scatter around model curves in Figure 12 should not be taken at face value.

We point out that the  $N_{\text{H}}$  in Figure 12 is proportional to  $R$ . Although this is our best estimate of  $N_{\text{H}}$  based on the correlation between the  $\gamma$ -ray data and gas templates, we did not measure the  $N_{\text{H}}$  distribution on pixel scales. Accordingly, overinterpretation of Figure 12 (e.g., estimating the  $T_{\text{S}}$  and the excess gas column density on very small scales) should be avoided.

The average column density of the neutral gas ( $\overline{N_{\text{H}}}$ ) in the northern region is obtained as  $\sim 3.4 \times 10^{20} \text{ cm}^{-2}$  based on either  $W_{\text{HI}}$  (with optically thin approximation) or  $R$  (with the conversion factor determined in Section 2.2). On the other hand, that based on  $\tau_{353}$  is  $\sim 4.3 \times 10^{20} \text{ cm}^{-2}$ , indicating that an  $N_{\text{H}} \propto \tau_{353}$  model (not favored by  $\gamma$ -ray analysis) overestimates the gas column density by  $\sim 30\%$ . In the southern region, again, while the values of  $\overline{N_{\text{H}}}$  inferred by  $W_{\text{HI}}$  and  $R$  are similar ( $\sim 2.2 \times 10^{20} \text{ cm}^{-2}$ ), that based on  $\tau_{353}$  is  $\sim 15\%$  higher. This supports our earlier statement that the use of the  $\gamma$ -ray data is crucial to accurately determine the  $N_{\text{H}}$  distribution.

### 5.2. CRs in the Local Environment

Next, we discuss the HI emissivity spectra obtained in this study, which are summarized in Figure 13(a) and (b). To investigate possible systematic uncertainties due to the choice of the  $N_{\text{H}}$  template and the IC model, in the northern region (where the normalization of the IC model is  $\sim 0$  for all six models) we bracketed the spectrum with that obtained using the  $N_{\text{H}}$  model based on  $W_{\text{HI}}$  (i.e., the pure optically thin HI scenario) and with that obtained using the  $N_{\text{H}}$  model based on  $R$  but with the normalization of the IC model fixed to 1.0. For the southern region, we bracketed the spectrum those obtained using all six IC models. We also took into account the LAT effective area uncertainty<sup>19</sup>; we assumed the uncertainty to be 10% below 200 MeV (where we used only events of PSF classes 2 and 3) and 5% above 200 MeV. The fractional uncertainties of the spectrum due to the modeling ( $N_{\text{H}}$  and IC for the northern and southern regions, respectively) and that due to the effective area uncertainty are summed in quadrature and shown as shaded bands; they are 11%–13% below 200 MeV and  $\lesssim 10\%$  above 200 MeV. For comparison, we plotted the model curve for the LIS that we adopted with  $\epsilon_{\text{M}}$  of 1.84 in the same figure. In order to approximately indicate the uncertainty in the emissivity model (primarily due to the uncertainty in the elemental composition of the CRs and the cross sections other than for proton–proton (p–p) collisions), we also plotted the model curve for  $\epsilon_{\text{M}} = 1.45$  (the lowest value referred to in Mori 2009), which gives 15%–20% lower emissivity. We also plotted the emissivity spectrum of the same ROI measured by Abdo et al. (2009b) using six months of *Fermi*-LAT data. Our results favor the model curve with  $\epsilon_{\text{M}} = 1.84$  and agree well with those by Abdo et al. (2009b), but here we cover a wider energy range and investigate northern/southern regions separately. In other words, the analysis presented here shows for the first time that the HI emissivities are consistent between the northern and southern regions at the 10% level, supporting the hypothesis that the CR intensity is uniform in the vicinity of the solar system. The integral emissivities above 100 MeV are  $(1.58 \pm 0.04) \times 10^{-26}$  photons  $\text{s}^{-1} \text{sr}^{-1} \text{H-atom}^{-1}$  and  $(1.59 \pm 0.02) \times 10^{-26}$  photons  $\text{s}^{-1} \text{sr}^{-1} \text{H-atom}^{-1}$  in the northern and southern regions, respectively, and those above 300 MeV are  $(0.68 \pm 0.01) \times 10^{-26}$  photons  $\text{s}^{-1} \text{sr}^{-1} \text{H-atom}^{-1}$  and  $(0.69 \pm 0.01) \times 10^{-26}$  photons  $\text{s}^{-1} \text{sr}^{-1} \text{H-atom}^{-1}$  in the northern and southern regions, respectively, with an additional systematic error of  $\sim 10\%$  due to the modeling and the effective area uncertainties (see above). We also note that our emissivities agree (within  $\leq 10\%$ ) with the results of by Shen et al. (2019), where the authors analyzed the same northern region employing a template-fitting method with the assumption of a uniform  $T_{\text{S}}$  for the atomic gas phase and discussed the local CR spectrum based on recent p–p interaction models and AMS–02 data. In other words, our analysis supports their findings by showing that  $T_{\text{S}} = 125$  K is compatible with most of the  $N_{\text{H}}$  distribution and that the CR spectrum is uniform.

As in the case of discussing the ISM gas densities (Section 5.1), evaluating the gas model using the  $\gamma$ -ray data is crucial to accurately constrain the HI emissivity and CR intensity. If we use the  $N_{\text{H}} \propto \tau_{353}$  models, the scale factors of the HI emissivity ( $\propto$  CR intensity) are 30%–40% lower (see Sections 4.1.1 and 4.2.1). Other source of uncertainty on the CR intensity are the hadronic interaction cross section and the elemental composition of CRs as indicated by two curves ( $\epsilon_{\text{M}} = 1.84$  and 1.45) in Figure 13(a). If we adopt  $\epsilon_{\text{M}} = 1.45$ , we would need  $\sim 25\%$  higher proton LIS flux, which might be incompatible with the proton flux directly measured at the Earth. Given the uncertainty and

<sup>19</sup> [http://fermi.gsfc.nasa.gov/ssc/data/analysis/LAT\\_caveats.html](http://fermi.gsfc.nasa.gov/ssc/data/analysis/LAT_caveats.html)



the fact that the directly measured CRs do not necessarily represent the LIS, we do not deny such a possibility. See discussions in, e.g., [Strong \(2015\)](#), [Orlando \(2018\)](#), and [Shen et al. \(2019\)](#). In Figure 13(a), one may also recognize that the model overestimates the data below a few 100 MeV while it predicts lower flux above 1 GeV. This might indicate a possible spectral break of the proton LIS. For example, [Strong \(2015\)](#) reported a break at a few GeV based on [Casandjian \(2015\)](#) that gives a similar spectrum to ours (see also Figure 13(b)). To reach a robust conclusion, constraining the electron LIS using radio synchrotron emission (e.g., [Orlando 2018](#)) and an accurate determination of the emissivity spectrum below a few 100 MeV is crucial. Because the analysis suffers from coupling with the point sources through IC model in low-energy bands (see Section 4.1.1), we defer such a study to future projects using gas-rich areas.

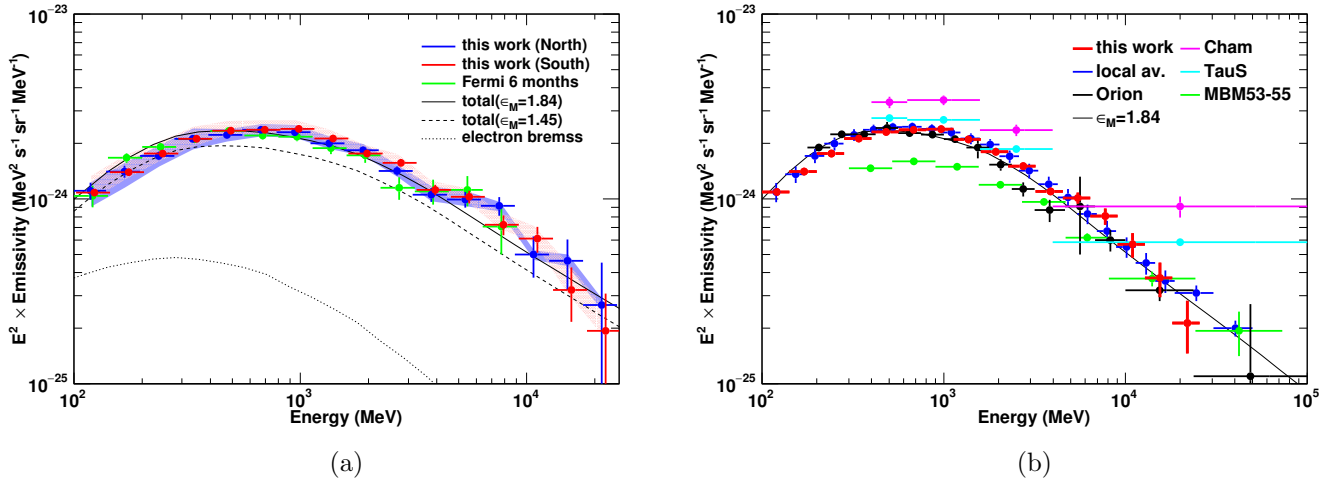


**Figure 13.** (a) Summary of the H I emissivity spectra of the northern and southern regions. They are compared with the model curves based on the LIS for  $\epsilon_M = 1.45$  and  $1.84$ , and the result of the relevant study by *Fermi*-LAT based on six months of observation ([Abdo et al. 2009b](#)). The contribution of the electron bremsstrahlung is also shown. The shaded bands show the systematic uncertainties of the spectrum (see the text in Section 5.2 for details). (b) The average of the H I emissivity spectra obtained in this study compared with previous *Fermi*-LAT results for high latitude areas. Errors are statistical only.

Finally, we compare our H I emissivity spectrum (the average of the northern and southern regions) with several other *Fermi*-LAT studies of nearby clouds: the average spectrum found in the local ISM in  $10^\circ \leq |b| \leq 70^\circ$  by [Casandjian \(2015\)](#), that toward the Orion molecular clouds by [Ackermann et al. \(2012c\)](#), that toward the Chamaeleon molecular clouds by [Planck Collaboration Int. XXVIII \(2015\)](#), that toward the South Taurus cloud by [Remy et al. \(2017\)](#), and that toward the MBM 53, 54, 55 clouds and the Pegasus loop by [Mizuno et al. \(2016\)](#), as summarized in Figure 13(b). Although the spectral shape does not change significantly over the samples examined here, the peak-to-peak variation of the normalization is by a factor of  $\sim 2$  even in nearby clouds. Given the diffusive nature of the Galactic CRs, and the lack of significant change of the spectral shape, the variation is mostly attributable to uncertainties of the gas column density, particularly due to assumptions of the value of  $T_s$ . For example, as discussed by [Planck Collaboration Int. XXVIII \(2015\)](#), the emissivity toward the Chamaeleon clouds agrees with that found by [Casandjian \(2015\)](#) within  $\sim 20\%$  if we assume

$T_S = 140$  K for HI clouds, although the  $\gamma$ -ray fit favors higher  $T_S$ . A small gradient at the 20% level could be possible and of interest to understand the CR generation and propagation in the vicinity of the solar system, and a systematic study of nearby clouds is therefore important. In such future studies, one should overcome the uncertainty on the  $N_H$  distribution by using the HI, CO, and dust data together with GeV  $\gamma$ -rays as a robust tracer of the ISM gas.

## 6. SUMMARY AND FUTURE PROSPECTS

We performed a detailed study of the ISM and CRs in the mid-latitude region of the third quadrant using the *Fermi*-LAT data in the 0.1–25.6 GeV range and other interstellar gas tracers such as the HI4PI survey and the *Planck* dust model. Even though this region was analyzed in an early publication of the *Fermi*-LAT collaboration using six months of data, the analysis was significantly improved using eight years of *Fermi*-LAT data with the aid of newly available gas tracers and with the northern and southern regions treated separately. We used  $\gamma$ -rays as a robust tracer of the ISM gas and examined possible variations of the  $N_{\text{H}}/D_{\text{em}}$  ratio. We tested several IC models and confirmed that the effect on the  $N_{\text{H}}/D_{\text{em}}$  ratio is at the 10% level, and also confirmed that the uncertainty of the Sun/Moon emission model does not affect the gas component. We found that dust opacity at 353 GHz increases in low  $T_{\text{d}}$  or high density areas for the northern and southern regions, respectively. On the other hand, the  $\gamma$ -ray analysis preferred the  $R$ -based  $N_{\text{H}}$  template in both northern and southern regions, and we adopted  $R$ -based  $N_{\text{H}}$  models as our best estimate of the  $N_{\text{H}}$  distribution. While most of the gas can be interpreted as being HI of  $T_{\text{S}} = 125$  K or higher, an area of optically thick HI of  $T_{\text{S}} \sim 40$  K was revealed and possible CO-dark  $\text{H}_2$  was identified. The measured integrated  $\gamma$ -ray emissivities above 100 MeV were found to be  $(1.58 \pm 0.04) \times 10^{-26}$  photons  $\text{s}^{-1} \text{sr}^{-1} \text{H-atom}^{-1}$  and  $(1.59 \pm 0.02) \times 10^{-26}$  photons  $\text{s}^{-1} \text{sr}^{-1} \text{H-atom}^{-1}$  in the northern and southern regions, respectively, supporting the existence of uniform CR intensity in the vicinity of the solar system. Although our emissivity agrees with the calculation using the LIS model based on the directly measured CR proton spectrum with  $\epsilon_{\text{M}} = 1.84$ , we caution that the uncertainty of the  $\gamma$ -ray emissivity model is still at the 20% level. The choice of the ISM gas tracer and the correction of the  $N_{\text{H}}$  model using  $\gamma$ -ray data are crucial to accurately measure the ISM gas distribution and investigate the CR intensity. As discussed by Mizuno et al. (2016), the  $N_{\text{H}}/D_{\text{em}}$  ratio was found to depend on  $T_{\text{d}}$  in the MBM 53, 54, and 55 clouds and the Pegasus loop through  $\gamma$ -ray data analysis. Now we find, through this study, that the  $N_{\text{H}}/\tau_{353}$  ratio depends also on  $\tau_{353}$  as predicted by several dust evolution models. In the present study we demonstrated that, in order to accurately measure the ISM gas distribution and study the CR intensity and spectrum, the dependence on both  $T_{\text{d}}$  and  $D_{\text{em}}$  needs to be taken into account and a detailed examination of the  $W_{\text{HI}}-D_{\text{em}}$  relationship is required. This work may serve as a reference for future studies of nearby HI/CO clouds.

The *Fermi* LAT Collaboration acknowledges generous ongoing support from a number of agencies and institutes that have supported both the development and the operation of the LAT as well as scientific data analysis. These include the National Aeronautics and Space Administration and the Department of Energy in the United States, the Commissariat à l’Energie Atomique and the Centre National de la Recherche Scientifique / Institut National de Physique Nucléaire et de Physique des Particules in France, the Agenzia Spaziale Italiana and the Istituto Nazionale di Fisica Nucleare in Italy, the Ministry of Education, Culture, Sports, Science and Technology (MEXT), High Energy Accelerator Research Organization (KEK) and Japan Aerospace Exploration Agency (JAXA) in Japan, and the K. A. Wallenberg Foundation, the Swedish Research Council and the Swedish National Space Board in Sweden.

Additional support for science analysis during the operations phase is gratefully acknowledged from the Istituto Nazionale di Astrofisica in Italy and the Centre National d’Études Spatiales in France. This work performed in part under DOE Contract DE-AC02-76SF00515.

We would like to thank the referee for his/her valuable comments. This work was partially supported by JSPS Grants-in-Aid for Scientific Research (KAKENHI) Grant Numbers JP17H02866 (T. M.) and JP26800160 (K. H.), and Core Research Energetic Universe in Hiroshima University.

Some of the results in this paper have been derived using the HEALPix (Górski et al. 2005) package.

*Facilities:* Fermi, Planck, WMAP, Parkes, Effelsberg

*Software:* *Fermi* Science Tools (<http://fermi.gsfc.nasa.gov/ssc/data/analysis/software/>), GALPROP (Strong & Moskalenko 1998; Strong et al. 2007), HEALPix (Górski et al. 2005), ROOT (<https://root.cern.ch>)

## APPENDIX

A. VELOCITY-SORTED  $W_{\text{HI}}$  MAPS

The velocity-sorted  $W_{\text{HI}}$  maps are summarized in Figures 14 and 15 for the northern and southern regions, respectively. As shown in the panels (a) and (d) of Figure 14, most of the gas is local (the velocity  $|v| \leq 35 \text{ km s}^{-1}$ ) in the northern region. Three bright radio continuum sources ( $W_{\text{HI}} \geq 50 \text{ K km s}^{-1}$ ) are seen in  $|v| \geq 70 \text{ km s}^{-1}$  at  $(l, b)$  around  $(246^\circ.1, 39^\circ.9)$ ,  $(233^\circ.2, 43^\circ.8)$ , and  $(208^\circ.6, 44^\circ.5)$ . They were removed by filling the source areas with the average of the peripheral pixels: values in a circular region with radius  $0.4$  are filled with the average of pixels in a ring with inner radius of  $0.4$  and outer radius of  $0.5$  in the  $W_{\text{HI}}$  map. The parameters (position and radius) are summarized in Table 7.

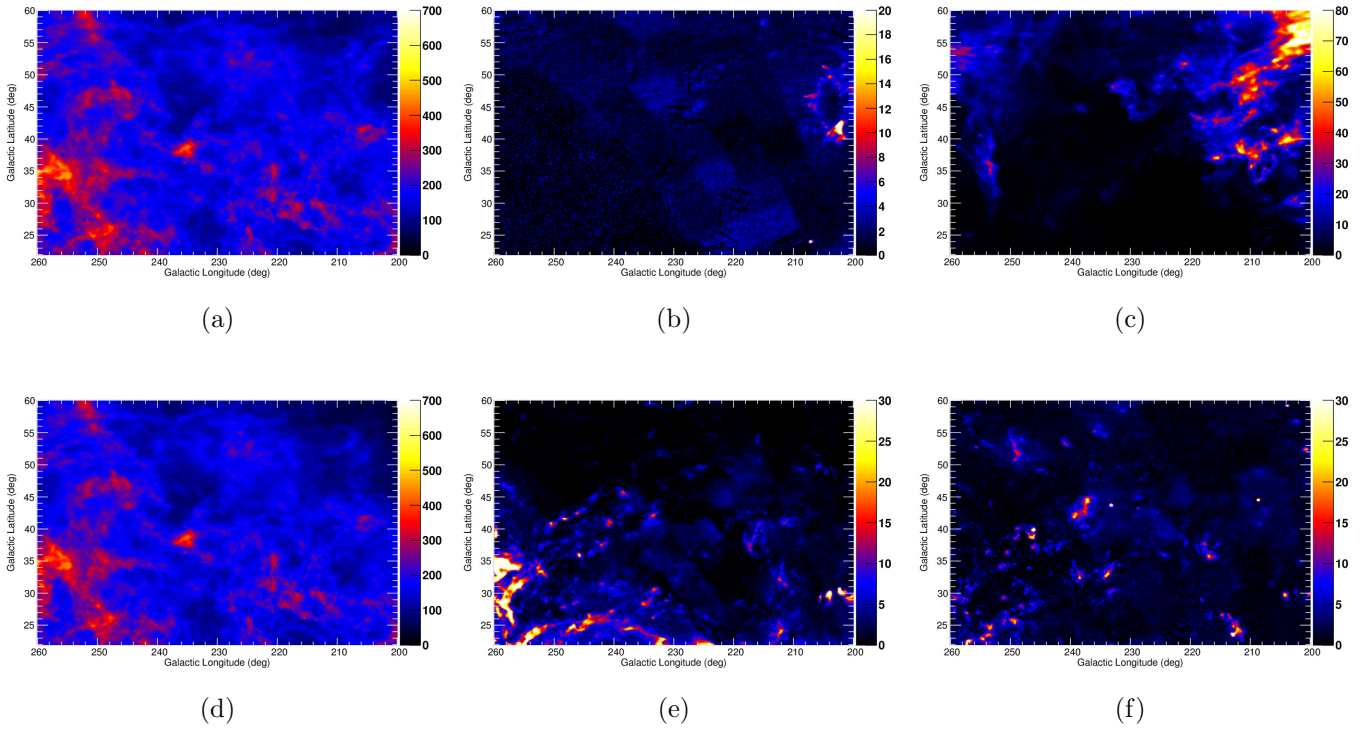


**Figure 14.**  $W_{\text{HI}}$  maps ( $\text{K km s}^{-1}$ ) in the northern region (a) integrated over the whole velocity range (from  $-600$  to  $+600 \text{ km s}^{-1}$ ) and in the velocities (b) from  $-600$  to  $-70 \text{ km s}^{-1}$ , (c) from  $-70$  to  $-35 \text{ km s}^{-1}$ , (d) from  $-35$  to  $35 \text{ km s}^{-1}$ , (e) from  $+35$  to  $+70 \text{ km s}^{-1}$ , and (f) from  $+70$  to  $+600 \text{ km s}^{-1}$ .

In the southern region, while most of the gas is in local ( $|v| \leq 35 \text{ km s}^{-1}$ ), we can identify a coherent structure in  $238^\circ \leq l \leq 246^\circ$  and  $-53^\circ \leq b \leq -48^\circ$  in  $v$  from  $-70$  to  $-35 \text{ km s}^{-1}$ ; the structure is likely to be an intermediate velocity cloud (e.g., Wakker 2001). This area has a large scatter in  $W_{\text{HI}}$  while  $D_{\text{em}}$  is rather constant likely because of the contamination of the clouds. Because the scatter in  $W_{\text{HI}}$  would affect the  $W_{\text{HI}}-D_{\text{em}}$  correlation (Section 2.2), we masked the area in the study of the  $W_{\text{HI}}-D_{\text{em}}$  relationship and  $\gamma$ -ray data analysis. We can also identify another coherent structure (HI cloud) in  $v$  from  $-70$  to  $-35 \text{ km s}^{-1}$  in  $200^\circ \leq l \leq 215^\circ$  and  $35^\circ \leq b \leq 60^\circ$  in the northern region. Because the structure shows the  $W_{\text{HI}}-D_{\text{em}}$  relationship similar to those in other regions, we did not mask the area

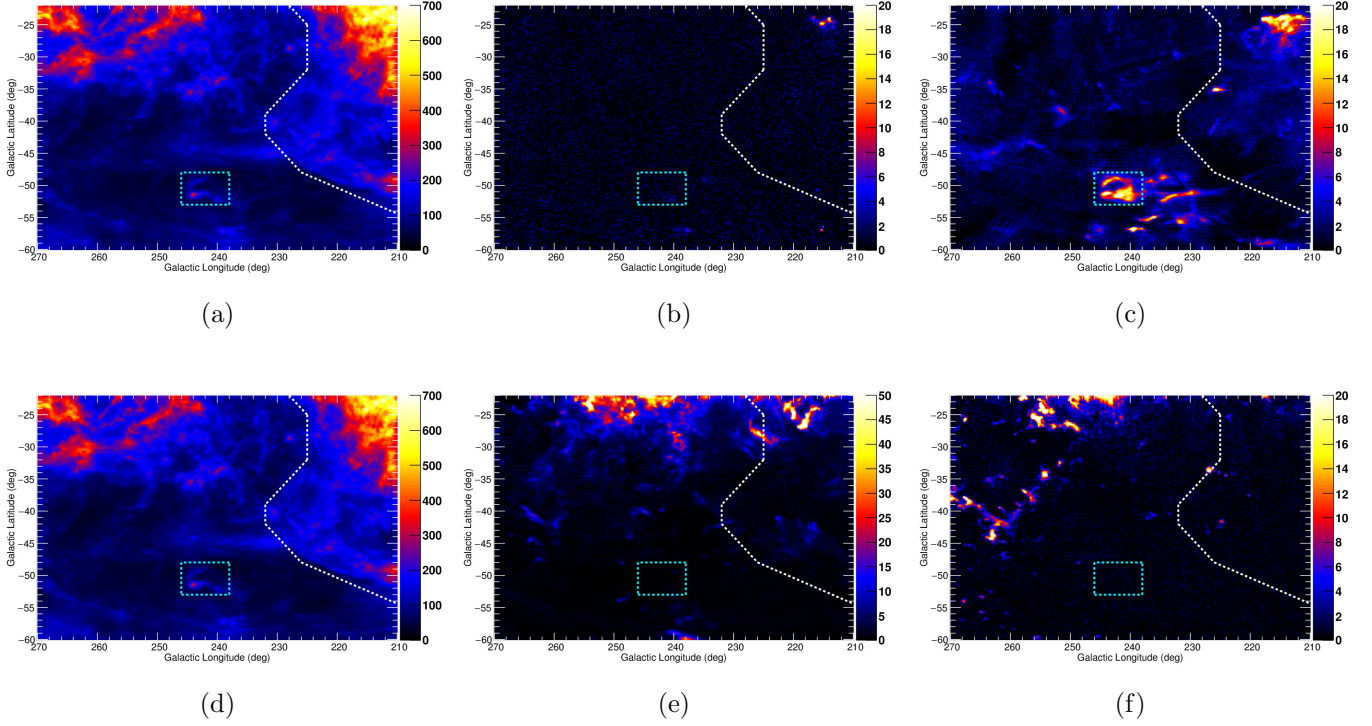


**Figure 15.** The same as Figure 15 but for the southern region. The intermediate velocity cloud and the Orion-Eridanus superbubble are masked by areas shown by dotted lines (see text for details).

to maximize the photon statistics in  $\gamma$ -ray data analysis. The relative contribution of the HI cloud to the  $\gamma$ -ray flux (assuming uniform CR intensity) and the mass of the ISM gas (assuming the same distance) can be evaluated by integrating  $W_{\text{HI}}$  in the ROI. The relative contribution of this structure (integrated from  $-70$  to  $-35$   $\text{km s}^{-1}$  in  $200^\circ \leq l \leq 215^\circ$  and  $35^\circ \leq b \leq 60^\circ$ ) to the whole emission of  $W_{\text{HI}}$  in the northern region was found to be only  $\leq 2\%$ ; therefore the effects on the evaluated CR emissivity and  $N_{\text{H}}$  are, if any, negligible. The contributions of local clouds (integrated from  $-35$  to  $35$   $\text{km s}^{-1}$  in each ROI) to the whole emission are more than 93% and 94% for the northern and southern regions, respectively.

The Orion-Eridanus superbubble (e.g., Ochsendorf et al. 2015) can be identified as filamentary structures in HI 21-cm and  $\text{H}\alpha$  lines. To visualize the superbubble, we made a  $W_{\text{HI}}$  map in  $v = -1$  to  $8$   $\text{km s}^{-1}$  (Brown et al. 1995) and an  $\text{H}\alpha$  map (Finkbeiner 2003) in Figure 16. Since the CR and ISM properties of the structure could be appreciably different from those of other regions, the area of the superbubble was masked in the study of the  $W_{\text{HI}}-D_{\text{em}}$  relationship and  $\gamma$ -ray data analysis with a polygon defined by  $(l, b) = (228^\circ, -22^\circ), (225^\circ, -25^\circ), (225^\circ, -32^\circ), (232^\circ, -39^\circ), (232^\circ, -42^\circ), (226^\circ, -48^\circ),$  and  $(210^\circ, -54.4^\circ)$ . Indeed, the masked area shows a different  $W_{\text{HI}}-D_{\text{em}}$  relation from other areas in the ROI.



**Table 7.** Radio and infrared sources excised and interpolated in the  $W_{\text{HI}}$  map and *Planck* dust maps.

Position		$r_1$	$r_2$	Object type
$l$ (deg)	$b$ (deg)	(deg)	(deg)	
255.5	52.8	0.12	0.15	infrared source
246.1	39.9	0.4	0.5	radio source
241.7	-36.5	0.12	0.15	infrared source
241.2	-35.9	0.12	0.15	infrared source
238.0	-54.6	0.12	0.15	infrared source
233.2	43.8	0.4	0.5	radio source
221.4	45.1	0.12	0.15	infrared source
214.1	47.8	0.12	0.15	infrared source
208.7	44.5	0.12	0.15	infrared source
208.6	44.5	0.4	0.5	radio source

NOTE— Values in a circular region with a radius of  $r_1$  are filled with the average of pixels in a ring with inner radius of  $r_1$  and outer radius of  $r_2$  for each position.

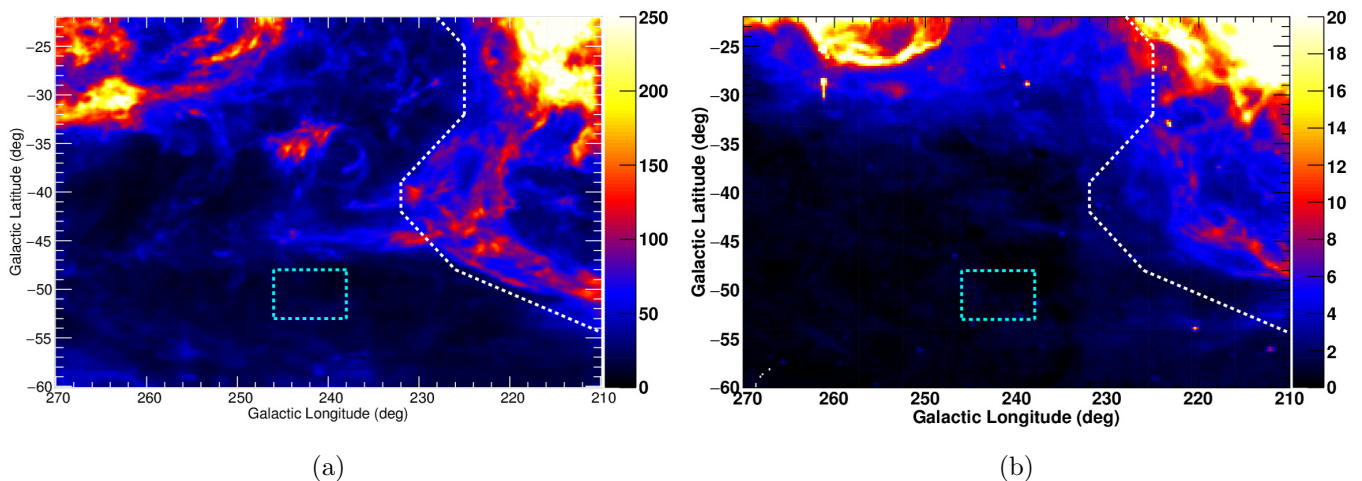


**Figure 16.**  $W_{\text{HI}}$  map in the southern region in the velocities from  $-1$  to  $8 \text{ km s}^{-1}$  (Brown et al. 1995) (a) and  $\text{H}\alpha$  map (Finkbeiner 2003) (b). The Orion-Eridanus superbubble can be identified as filamentary structures in those maps and is masked by the polygon shown as a dotted white line.

## B. INFRARED SOURCES

We compared the  $R$  and  $\tau_{353}$  maps and identified several spots of high  $R/\tau_{353}$  ratio ( $\geq 0.05 \text{ W m}^{-2} \text{ sr}^{-1}$ ) and high  $R$  ( $\geq 16 \times 10^{-8}$  and  $10 \times 10^{-8}$  in units of  $\text{W m}^{-2} \text{ sr}^{-1}$  in the northern and southern regions, respectively). Their positions are  $(l, b) = (241^\circ.7, -36^\circ.5)$ ,  $(241^\circ.2, -35^\circ.9)$ ,  $(238^\circ.0, -54^\circ.6)$ ,  $(214^\circ.1, 47^\circ.8)$ ,  $(255^\circ.5, 52^\circ.8)$ , and  $(208^\circ.7, 44^\circ.5)$ . We identified them as infrared sources and removed them by filling the source areas in the  $R$ ,  $\tau_{353}$ , and  $T_d$  maps with the average of the peripheral pixels: values in a circular region with radius  $0^\circ.12$  are filled with the average of the pixels in a ring with inner radius of  $0^\circ.12$  and outer radius of  $0^\circ.15$ . The parameters (position and radius) are also summarized in Table 7.

## C. PLANCK CO MAP

We also examined the Planck type 3 CO map (Planck Collaboration XIII 2014) and confirmed that there is no strong CO 2.6 mm emission in our ROI. In Figure 17(a), we identified emission of moderate intensity (peak intensity  $\sim 4 \text{ K km s}^{-1}$ ) at  $(l, b) \sim (221^\circ.4, 45^\circ.1)$ . It is also seen in the  $R$  and  $\tau_{353}$  maps and likely to be an infrared source, and was removed from the dust maps by filling in with the average value of peripheral pixels. The source is also listed in Table 7. Other bright CO 2.6 mm emission at around  $(l, b) = (211^\circ, -36^\circ.5)$  is inside the mask of the Orion-Eridanus superbubble, as shown in panel (b).

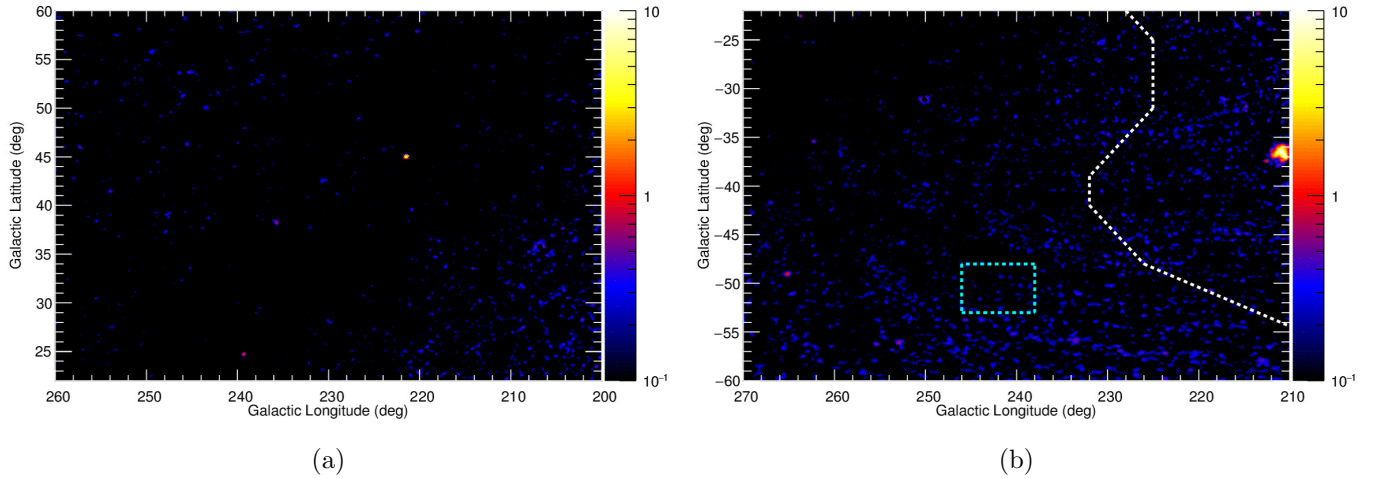


**Figure 17.** Planck type 3  $W_{\text{CO}}$  maps ( $\text{K km s}^{-1}$ ) in the (a) northern and (b) southern regions. The spot of moderate intensity at  $(l, b) \sim (221^\circ.4, 45^\circ.1)$  was removed from the dust maps used in the study. Other bright CO 2.6 mm emission seen in the southern region is inside the area that is masked (see Appendix A).

D.  $W_{\text{HI}}-D_{\text{em}}$  CORRELATION WITH FINER  $T_{\text{d}}$  BINS

In Section 2.1, we examined the  $T_{\text{d}}$  dependence of the  $W_{\text{HI}}-D_{\text{em}}(R \text{ or } \tau_{353})$  relationship in the six  $T_{\text{d}}$  bins, where the data are grouped in 1 K ranges of  $T_{\text{d}}$  (see Figures 1 and 2). In Figures 18 and 19 we show the same plots, but in which the data are grouped in 0.5 K ranges of  $T_{\text{d}}$  to reduce the overlapping of points in the plot at the expense of separating data into two plots to cover the whole  $T_{\text{d}}$  range.

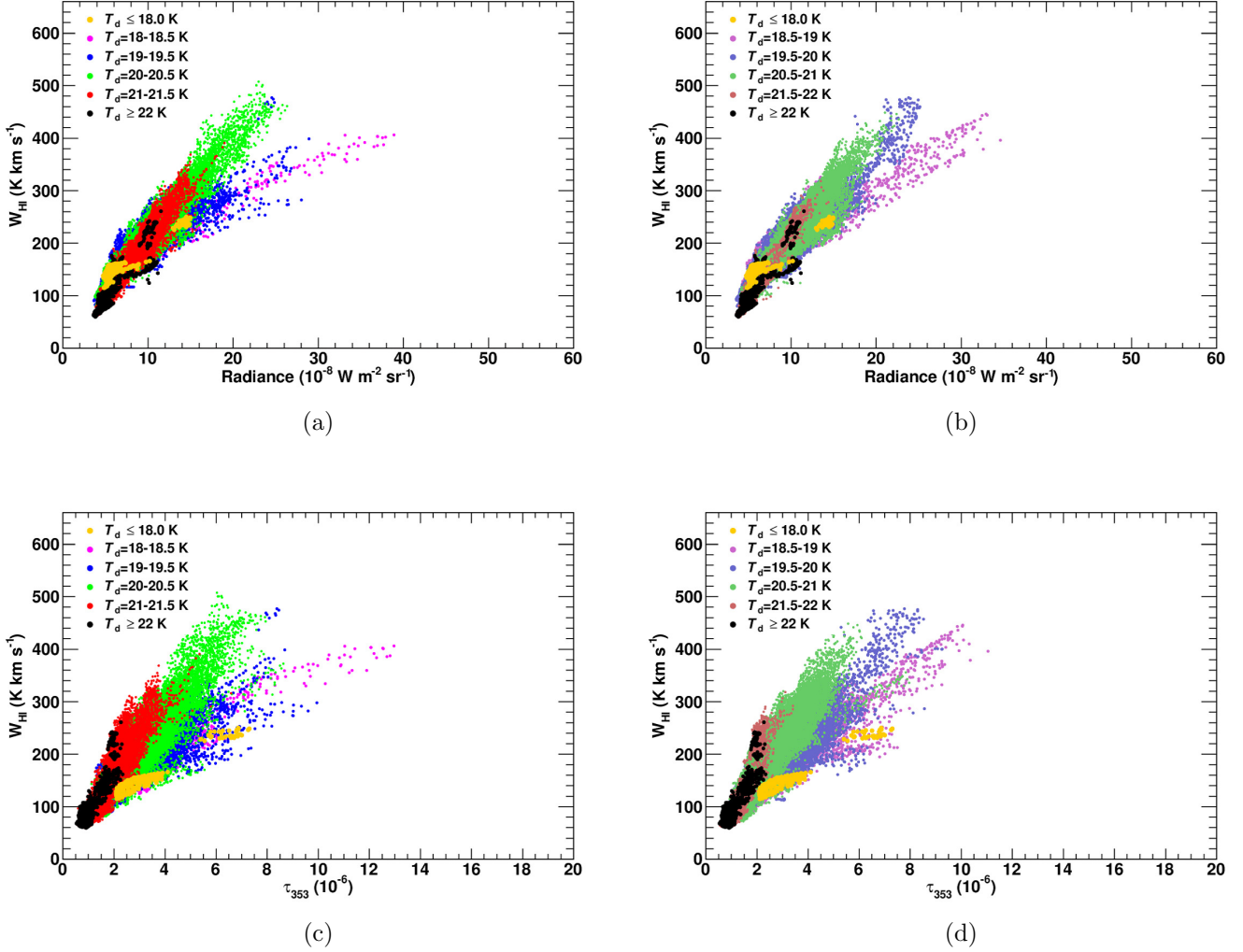


**Figure 18.** Correlation between  $W_{\text{HI}}$  and dust tracers in the northern region. Panels (a) and (b) show the  $W_{\text{HI}}-R$  relations and panels (c) and (d) show the  $W_{\text{HI}}-\tau_{353}$  relations.

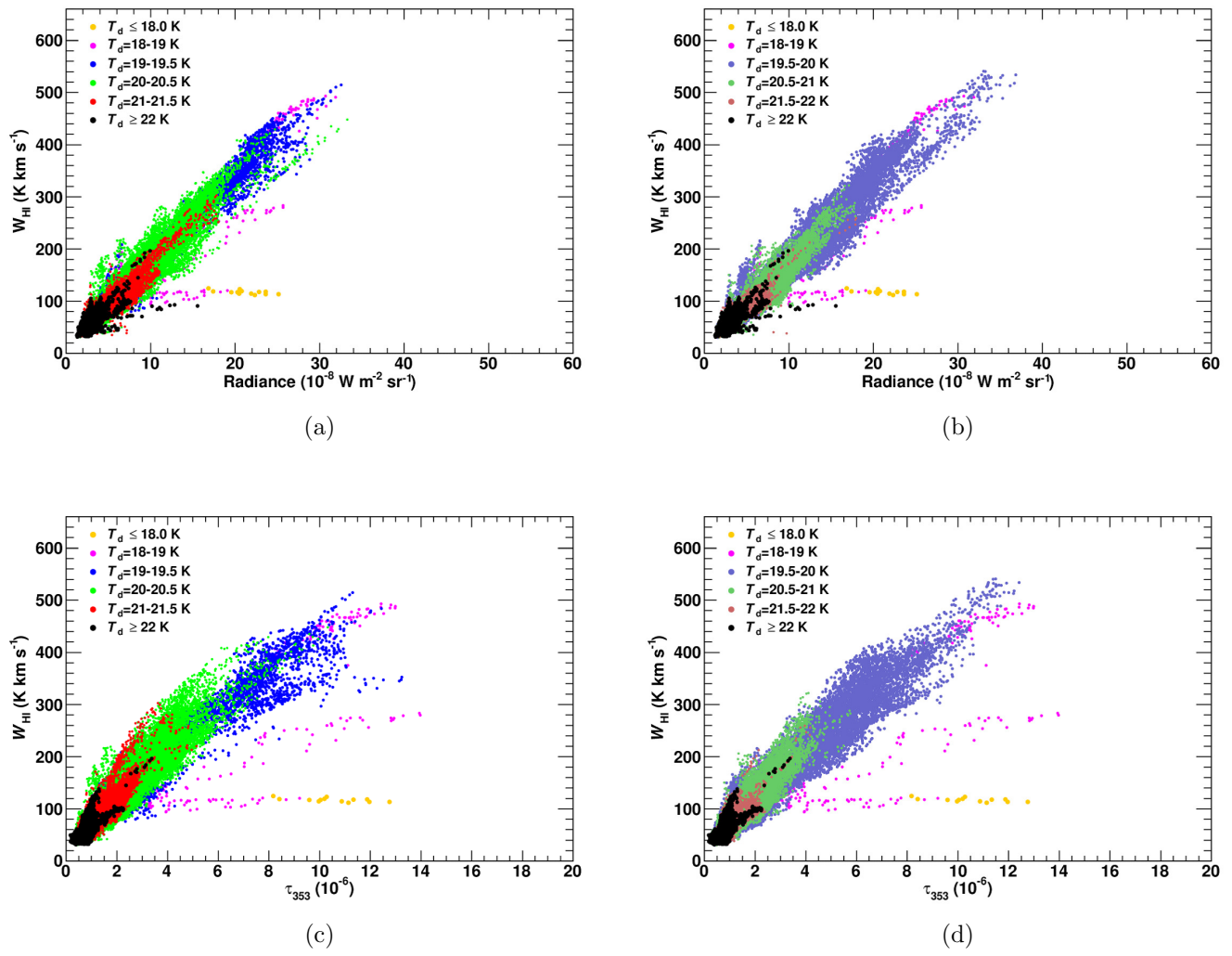


**Figure 19.** The same as Figure 18 but for the southern region.

## REFERENCES

- Abdo, A. A., Ackermann, M., Ajello, M., et al. 2009a, *Astropart. Phys.*, 32, 193
- Abdo, A. A., Ackermann, M., Ajello, M., et al. 2009b, *ApJ*, 703, 1249
- Abdo, A. A., Ackermann, M., Ajello, M., et al. 2010, *ApJ*, 710, 133
- Abo, A. A., Ackermann, M., Ajello, M., et al. 2011, *ApJ*, 734, 116
- Abdollahi, S., Acero, F., Ackermann, M., et al. 2019, arXiv:1902.10045
- Ackermann, M., Ajello, M., Baldini, L., et al. 2011, *ApJ*, 726, 81
- Ackermann, M., Ajello, M., Atwood, W. B., et al. 2012a, *ApJ*, 750, 3
- Ackermann, M., Ajello, M., Allafort, A., et al. 2012b, *ApJ*, 755, 22
- Ackermann, M., Ajello, M., Allafort, A., et al. 2012c, *ApJ*, 756, 4
- Ackermann, M., Ajello, M., Atwood, W. B., et al. 2015, *ApJ*, 810, 14
- Ackermann, M., Ajello, M., Albert, A., et al. 2016, *PhRvD*, 93, 082001
- Acero, F., Ackermann, M., Ajello, M., et al. 2015, *ApJS*, 23, 41
- Atwood, W. B., Abdo, A. A., Ackermann, M., et al. 2009, *ApJ*, 697, 1071
- Bennett, C. L., Larson, D., Weiland, J. L., et al. 2013, *ApJS*, 208, 20
- Bohlin, R. C., Savage, B. D., & Drake, J. F. 1978, *ApJ*, 224, 132
- Brown, A. G. A., Hartmann, D., Burton, W. B. 1995, *A&A*, 300, 903
- Casandjian, J.-M. 2015, *ApJ*, 806, 240
- Case, G. L., Bhattacharya, D. 1998, *ApJ*, 504, 761
- Dame, T. M., Hartmann, D., & Thaddeus, P. 2001, *ApJ*, 547, 792
- de Palma, F., Brandt, T. J., Johannesson, G., & Tibaldo, L. 2012, arXiv:1304.1395
- Dickey, J. M., & Lockman, F. J. 1990, *ARA&A*, 28, 215
- Ferriere, K. 2001, *Rev. of Mod. Phys.* 73, 1031
- Finkbeiner, D. P. 2003, *ApJS*, 146, 407
- Fukui, Y., Torii, K., Onishi, T., et al. 2015, *ApJ*, 798, 6
- Górski, K. M., Hivon, E., Banday, A. J., et al. 2005, *ApJ*, 622, 759
- Grenier, I. A., Casandjian, J.-M., & Terrier, R. 2005, *Science*, 307, 1292
- Grenier, I. A., Black, J. H., & Strong, A. W. 2015, *ARA&A*, 53, 199
- HI4PI Collaboration 2016, *A&A*, 594, 116
- Jones, A. P., Fanciullo, L., Köhler, M., et al. 2013, *A&A*, 558, 62
- Köhler, M., Ysard, N., & Jones, A. P. 2015, *A&A*, 579, 15
- Lorimer, D. R., Faulkner, A. J., Lyne, A. D., et al. 2006, *MNRAS*, 372, 777
- Mattox, J. R., Bertsch, D. L., Chiang, J., et al. 1996, *ApJ*, 461, 396
- Mizuno, T., Abdollahi, S., Fukui, Y., et al. 2016, *ApJ*, 833, 278
- Mori, K. 2009, *Astropart.Phys.*, 31, 341
- Moskalenko, I. V., Porter, T., Strong W. 2006, *ApJL*, 640, 155
- Ochsendorf, B. B., et al. 2015, *ApJ*, 808, 111
- Orlando, E. 2018, *MNRAS*, 475, 2724
- Planck Collaboration XIX 2011, *A&A*, 536, 19
- Planck Collaboration XI 2014, *A&A*, 571, 11
- Planck Collaboration XIII 2014, *A&A*, 571, 13
- Planck Collaboration Int. XXVIII 2015, *A&A*, 582, 31
- Planck Collaboration XXIX 2016, *A&A*, 586, 132
- Porter, T. A., Moskalenko, I. V., Strong, A. W., et al. 2008, *ApJ*, 682, 400
- Remy, Q., Grenier, I. A., Marchall, D. J., & Casandjian, M. 2017, *A&A*, 601, 78
- Roy, A. et al. 2013, *ApJ*, 763, 55
- Shen, Z. Q., et al. 2019, arXiv:1904.12264
- Smith, R. J., Glover, S. C. O., Clark, P., et al. 2014, *MNRAS*, 441, 1628
- Strong, A. W., & Moskalenko, I. 1998, *ApJ*, 509, 212
- Strong, A. W., Moskalenko, I.V., & Ptuskin, V. S. 2007, *ARA&A*, 57, 285
- Strong, A. W. 2015, *Proc. ICRC*, 34, 506
- Wakker, B. P. 2001, *ApJS*, 136, 463
- Ysard, N., Köhler, M., Jones, A., et al. 2015, *A&A*, 577, 110
- Yusifov, I., & Küçük, I. 2004, *A&A*, 422, 545